

UNIVERSITY OF CALIFORNIA

Los Angeles

Integrated Cryogenic Buffer Gas Beam, Linear Quadrupole Trap, and Time of Flight Mass  
Spectrometer for Low Temperature Ion-Molecule Chemistry

A dissertation submitted in partial satisfaction

of the requirements for the degree

Doctor of Philosophy in Physics

by

Gary Chen

2019

© Copyright by

Gary Chen

2019

ABSTRACT OF THE DISSERTATION

Integrated Cryogenic Buffer Gas Beam, Linear Quadrupole Trap, and Time of Flight Mass Spectrometer for Low Temperature Ion-Molecule Chemistry

by

Gary Chen

Doctor of Philosophy in Physics

University of California, Los Angeles, 2019

Professor Wes Campbell, Chair

The dissertation of Gary Chen is approved.

Eric Hudson

Paul Hamilton

James Larkin

Wes Campbell, Committee Chair

University of California, Los Angeles

2019

*Noodle and Nugget*

## CONTENTS

<b>List of Figures . . . . .</b>	<b>viii</b>
<b>Preface . . . . .</b>	<b>xii</b>
<b>Curriculum Vitae . . . . .</b>	<b>xiii</b>
<b>1 Introduction . . . . .</b>	<b>1</b>
1.1 Thesis Outline . . . . .	1
<b>2 The Cryogenic Buffer Gas Beam (CBGB) . . . . .</b>	<b>2</b>
2.1 Design . . . . .	4
2.1.1 Heat Load and Thermal Conductivity . . . . .	6
2.1.2 Gas Fill Lines . . . . .	9
2.2 Beam Density and Extraction . . . . .	12
2.3 Beam Velocity . . . . .	20
<b>3 Trapping and Cooling Ions . . . . .</b>	<b>25</b>
3.1 Ion Trapping . . . . .	25
3.2 Vacuum Requirements . . . . .	25
3.3 ${}^9\text{Be}^+$ Laser Cooling . . . . .	26
3.4 Time of Flight Mass Spectrometer (TOF-MS) . . . . .	28
3.5 Dual Species Loading . . . . .	28
<b>4 Pseudo-First Order Reaction . . . . .</b>	<b>32</b>
<b>5 <math>\text{Be}^+({}^2\text{S}_{1/2} / {}^2\text{P}_{3/2}) + \text{H}_2\text{O}</math> . . . . .</b>	<b>33</b>

5.1	Optical Control of Reactions between Water and Laser-Cooled Be <sup>+</sup> Ions . . . . .	33
5.1.1	Abstract . . . . .	33
<b>6</b>	<b>Be<sup>+</sup> + H<sub>2</sub>O/HOD/D<sub>2</sub>O . . . . .</b>	<b>40</b>
6.1	Isotope-selective chemistry in the Be <sup>+</sup> ( <sup>2</sup> S <sub>1/2</sub> ) + HOD → BeOD <sup>+</sup> / BeOH <sup>+</sup> + H/D reaction . . . . .	40
6.2	Abstract . . . . .	40
6.3	Introduction . . . . .	40
6.4	Experimental . . . . .	42
6.5	Results and Discussion . . . . .	46
6.6	Conclusion . . . . .	48
6.7	Notes . . . . .	49
6.8	Be <sup>+</sup> + HOD branching ratio . . . . .	51
<b>7</b>	<b>Be<sup>+</sup> + O<sub>2</sub> . . . . .</b>	<b>53</b>
<b>8</b>	<b>C<sup>+</sup> + H<sub>2</sub>O . . . . .</b>	<b>57</b>
8.1	Formyl Isomer Branching Ratio . . . . .	57
8.2	CO <sub>2</sub> Titration . . . . .	59
8.2.1	Be <sup>+</sup> + CO <sub>2</sub> . . . . .	61
8.2.2	C <sup>+</sup> + CO <sub>2</sub> . . . . .	62
8.2.3	Be <sup>+</sup> + C <sup>+</sup> + H <sub>2</sub> O with CO <sub>2</sub> . . . . .	64
8.3	<sup>15</sup> N <sub>2</sub> Titration . . . . .	67
8.3.1	Estimate Isomerization . . . . .	67
<b>9</b>	<b>Conclusion and Future Outlook . . . . .</b>	<b>68</b>

<b>A Average Dipole Orientation Theory (ADO)</b>	<b>69</b>
A.0.1 General Treatment of Adiabatic Capture Theory	69
A.0.2 Ion-Dipole Interaction	71
<b>B Statistical State Counting</b>	<b>76</b>
<b>References</b>	<b>77</b>

## LIST OF FIGURES

2.1	Schematic of target species entrainment within a buffer gas beam cell. With high densities of buffer gas particles, an introduced target species undergoes collisions with the buffer gas such that it cools. At high enough densities, flow dynamics cause the target species to become entrained in the buffer gas flow and are carried out of the cell with greater efficiency. . . . .	3
2.2	Cross sectional view of CBGB in solidworks. Components include copper sheath for PTR, aluminum radiation shield with chevron baffles, copper shield and experimental cell, and skimmer mounted in stem chamber. The baffles allow for gas to flow into the cold region of the beam apparatus, while preventing 300K black body radiation from hitting the inner shield and cell. . . . .	5
2.3	Cross sectional view of CBGB with side walls removed from the outer vacuum chamber, 40K aluminum radiation shield, and inner 4K cryopumping shield exposing the inner experimental cell. A skimmer is mounted in the stem region. . . . .	6
2.4	The water fill line, sealed by an ultratorr fitting and heated by nichrome wire. A shut off valve and vernier valve are used to regulate the flow of water into the buffer gas cell. . . . .	10
2.5	A kapton film serves as the back wall of the buffer gas cell with a hole punctured for the insertion of the water fill line. The kapton surface seals the back of the cell for a stronger forward beam, while limiting the heat load from a room temperature fill line, and resisting ice formation allowing for continuous and consistent operation with water for over 10 hours. . . . .	11

2.6 A) $\gamma$ extraction ratio, dotted red line indicates $\gamma = 1$ where hydrodynamic entrainment begins. B) Theoretical number density of buffer gas species within buffer gas cell. The density of target species introduced should stay under 1% of the buffer gas density. C) Number of collisions a target species particle would expect before extraction out of the cell, the dotted red line indicates 100 collisions before extraction when rotational degrees of freedom are characteristically thermalized. . . . .	13
2.7 $(1.12 \times 10^9)f - (2.75 \times 10^{10})$ . . . . .	15
2.8 Projected buffer gas beam densities with a Ne flow rate of 30SCCM with various distances of interest within the chamber. Optimal densities of entrained gasses hover around 0.1% of the buffer gas value shown here. . . . .	17
2.9 . . . . .	18
2.10 Fluorescence decays of loaded $\text{Be}^+$ ions exposed to a cold water beam with an inline shutter either opened, in green ( $\tau = 7.23 \times 10^{-3}\text{s}$ ) or closed, in blue ( $\tau = 6.37 \times 10^{-2}\text{s}$ ) . . . . .	19
2.11 Fluorescence decays of loaded $\text{Be}^+$ ions exposed to a cold water beam with an inline shutter opened, in green ( $\tau = 5.37 \times 10^{-2}\text{s}$ ) or closed, in red ( $\tau = 7.59 \times 10^{-3}\text{s}$ )	20
2.12 . . . . .	23
2.13 . . . . .	24
 3.1 Set of ion images taken at various 313nm powers with an algorithm that identifies individual ions . . . . .	26
3.2 Individual ions identified from images in figure 3.1. Integrated fluorescence counts shown for each image as well as averaged value in brackets. . . . .	27
3.3 P-state fraction curve fitted to incident laser power at a fixed detuning of $\omega_l = \omega_0 - \Gamma/2$ . . . . .	28
3.4 Dual ablation set up. . . . .	30

3.5	TOF trace of simultaneous Be and C ablation averaged over 10 shots. A soft A-ramp is applied after loading, ejecting any unintentionally loaded C <sub>n</sub> clusters.	31
5.1		38
5.2		39
6.1		43
6.2		44
6.3		44
6.4		45
6.5		45
6.6		50
7.1	A linear dependence on the rate constant for reaction 7.1 as a function of P state excitation. $k = (6 \pm 1) \times 10^{-11}P + (-0.03 \pm 0.16) \times 10^{-11}$	54
7.2	Shared fitting of trapped products with 14% p-state excitation.	54
7.3	Shared fitting of trapped products with 14% p-state excitation.	55
7.4	TOF traces for data taken with 14% p-state excitation at 0s and 200s showing no products at 0s, but distinct peaks for reaction products BeH <sup>+</sup> , BeOH <sup>+</sup> , and O <sub>2</sub> <sup>+</sup> .	55
7.5	TOF traces for data taken with 14% p-state excitation at 0s and 200s showing no products at 0s, but distinct peaks for reaction products BeH <sup>+</sup> , BeOH <sup>+</sup> , and O <sub>2</sub> <sup>+</sup> .	56
8.1	RGA showing purity of CO <sub>2</sub> introduced into chamber. Ratios of CO <sub>2</sub> peaks at <i>m/z</i> = 12, 16, 28, and 44 in agreement with table 8.2, with no conclusive evidence of contamination by any other gas.	60
8.2	TOF trace of laser-cooled Be <sup>+</sup> reacting with $\approx 1 \times 10^{-8}$ Torr CO <sub>2</sub> introduced via leak valve for 50 seconds.	61

8.3	Integrated ion signal of individual TOF traces normalized by $\text{Be}^+$ fluorescence at various $\text{CO}_2$ exposure times. . . . .	62
8.4	TOF trace of laser-cooled $\text{Be}^+$ and $\text{C}^+$ reacting with $\approx 1 \times 10^{-8}$ Torr $\text{CO}_2$ introduced via leak valve for 40 seconds. . . . .	63
8.5	Integrated ion signal of individual TOF traces normalized by total ion signal excluding $\text{Be}^+$ at various $\text{CO}_2$ exposure times. . . . .	63
8.6	$\text{C}^+$ and $\text{Be}^+$ loaded into the trap is reacted with $\text{H}_2\text{O}$ introduced from the beam. The gate valve is closed after 10 seconds and $\text{CO}_2$ is introduced via leak valve so that the $\text{COH}^+$ is titrated into $\text{CO}_2\text{H}^+$ . . . . .	65
8.7	$C = 0.58 \pm 0.02$ $k_{8.7} = ((6.1 \pm 1.5) \times 10^{-10})\text{cm}^3/\text{s}$ . . . . .	67
A.1	Rough plotting of $\theta_1$ as a function of maximum angle $K$ . The behaviour is as expected, the greater the maximal capture angle, the more $\theta_1$ tends towards 0. . .	73
A.2	$\theta_2$ as a function of the ratio of rotational energy and the monopole-dipole term. The low ratio behavior is not immediately obvious, but the greater the ratio between the rotational energy and monopole-dipole term, the more $\theta_2$ tends towards $\pi/2$ . . . . .	74

## PREFACE

## CURRICULUM VITAE

- 2009 – 2013                    B.S. in Physics, University of Maryland (UMD), College Park, Maryland
- 2013 – Present                Ph.D. student in Physics, University of California, Los Angeles (UCLA).

# **CHAPTER 1**

## **Introduction**

This thesis chronicles the experimental work done to realize an apparatus for cold ion-molecule chemistry of species of astrochemical interest.

### **1.1 Thesis Outline**

## CHAPTER 2

### The Cryogenic Buffer Gas Beam (CBGB)

To reach reaction temperatures in the regime of 10K from a beam of molecules with trapped ions, a cryogenic buffer gas beam (CBGB) of neon with entrained water is employed. Numerous other methods of creating cold beams of molecules exist, from Zeeman decelerators [31], to Stark decelerators. CBGB's in particular have the benefit of being species agnostic, where the resultant beam properties are not dependent on the target species at hand, rather, the buffer gas species.

By holding a cell filled with a noble gas above its vapor pressure, a volume of gas can be held at cryogenic temperatures. Other species of molecules or atoms may be introduced into the buffer gas cell via ablation, fill line, etc. The target species particles are then sympathetically cooled via collisions with the cold buffer gas. An aperture at one end of the cell allows for the extraction of the buffer gas and entrained target species into a ballistic beam. Holding the buffer gas cell temperature to above 17K for neon, and 4K for helium, in high vacuum allows us to accumulate an appreciable stagnation number density within the cell to produce a beam of entrained target particles.

The Reynolds number is typically used to characterize the flow regime of the buffer gas beam. At the aperture of the buffer gas cell, the Reynolds number can be written as:

$$Re \approx \frac{2d_{\text{aperture}}}{\lambda} \approx \frac{8\sqrt{2}\dot{N}\sigma}{d_{\text{aperture}}\bar{v}} \quad (2.1)$$

Where  $d_{\text{aperture}}$  is the diameter of the aperture and  $\lambda$  is the mean free path of the buffer gas



Missing  
figure

Schematic of CBGB

Figure 2.1: Schematic of target species entrainment within a buffer gas beam cell. With high densities of buffer gas particles, an introduced target species undergoes collisions with the buffer gas such that it cools. At high enough densities, flow dynamics cause the target species to become entrained in the buffer gas flow and are carried out of the cell with greater efficiency.

particles.[22] When the Reynolds number is low,  $Re < 1$ , we find that there are on average  $> 1$  collisions at the aperture, meaning the particles escape with little to no interactions with other particles and is called the effusive regime. At high Reynolds numbers,  $Re > 100$ , in the supersonic regime, there are many collisions and forward velocity boosting as well as internal velocity distribution narrowing occurs. In between, we find the intermediate regime, where we observe the onset of hydrodynamic entrainment of target species with mild forward velocity boosting. In all cases, the gasses inside the cell at thermal equilibrium follow the Maxwell-Boltzmann distribution.

$$f(v) = \left( \frac{m}{2\pi kT} \right)^{3/2} 4\pi v^2 e^{-\frac{mv^2}{2kT}} \quad (2.2)$$

Where the mean velocity is:

$$\bar{v} = \sqrt{\frac{8k_B T}{\pi m}} \quad (2.3)$$

## 2.1 Design

The CBGB apparatus design has various stages, a room temperature 300K outer aluminum vacuum chamber, onto which a Pulse Tube Refrigerator (PTR) is mounted, an aluminum radiation shield mounted to the 40K PTR cooling stage, and an inner copper cryopumping shield and experimental cell connected to the 4K PTR cooling stage. Connected to the vertical vacuum chamber, a "stem" region protrudes out from the beam side as seen in figures figs. 2.2 and 2.3 where a large turbo V551pumps down the entire volume. The beam [turbo] comes out of the experimental cell and shield, through a set of apertures, into the stem [deets] region where skimmers and shutters are mounted to manipulate the beam.

A Cryomech PT415 PTR with a remote head option was attached to the top plate of the vacuum chamber with a large bellows mount to isolate the chamber from the mechanical vibrations caused by the PTR motor head. The chamber was pumped down to normal operating pressures, where then 4 retaining screws were tightened to just above the bellow's compressed height. This maintains mechanical decoupling between the outer vacuum chamber and the PTR while running.

We want to minimize the mechanically coupling onto the PTR due to the fragility of the pulse tube walls; small amounts of force applied onto a mechanically connected component would risk torquing the walls to break. Thus, all components inside the CBGB are mechanically connected to the top plate of the vacuum chamber via 8-32 stainless steel (SS316) threaded rods. Thermal connections are made with copper braids welded onto L-shaped brackets that mount between platforms secured to the PTR cooling stages and the shields.

Not only are all the inner shields connected to the top plate, but so are the feedthroughs including gas fill lines. This ensures that any and all connections made into the CBGB are not disturbed when opening the outer vacuum chamber to expose the inner components.

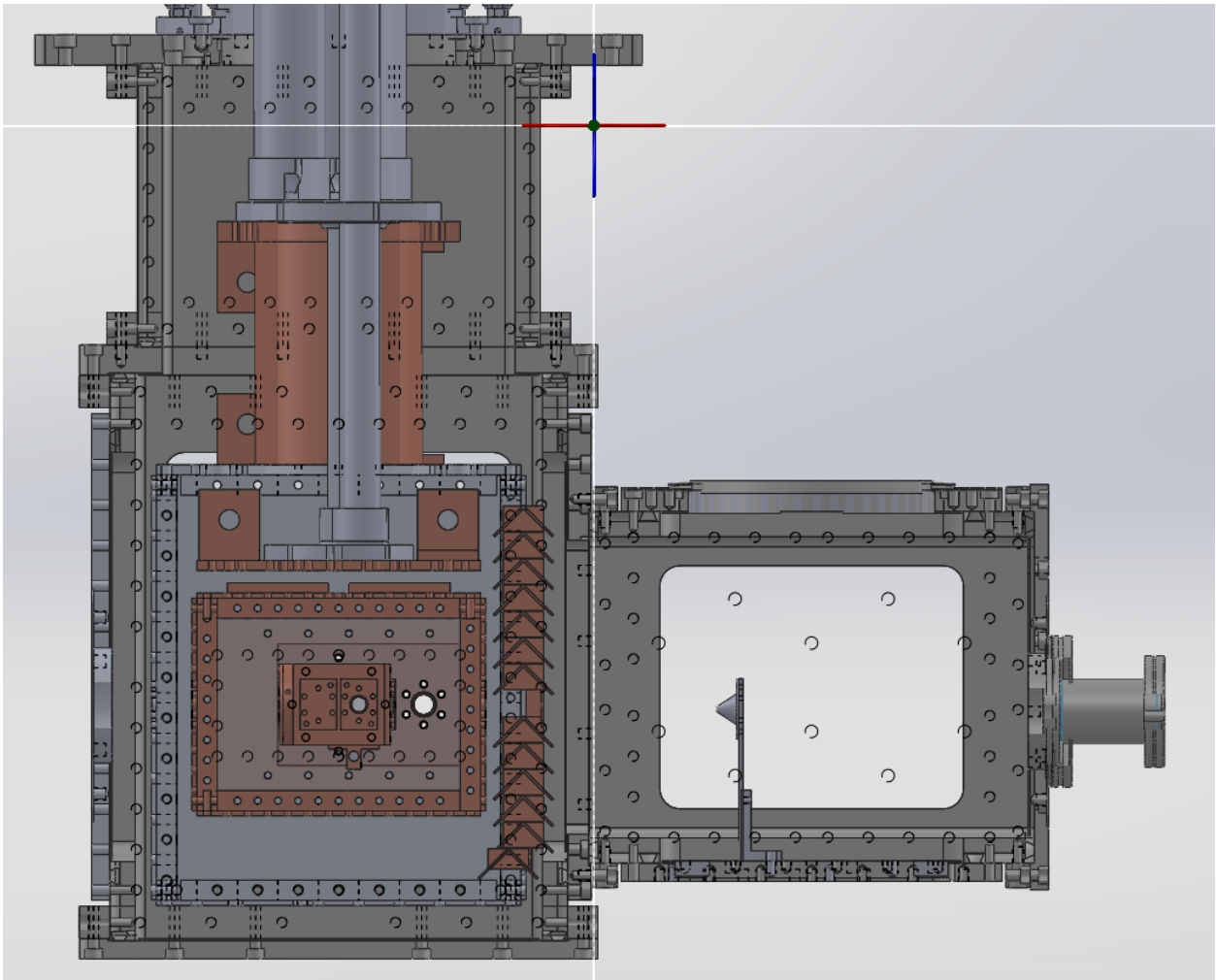


Figure 2.2: Cross sectional view of CBGB in solidworks. Components include copper sheath for PTR, aluminum radiation shield with chevron baffles, copper shield and experimental cell, and skimmer mounted in stem chamber. The baffles allow for gas to flow into the cold region of the beam apparatus, while preventing 300K black body radiation from hitting the inner shield and cell.

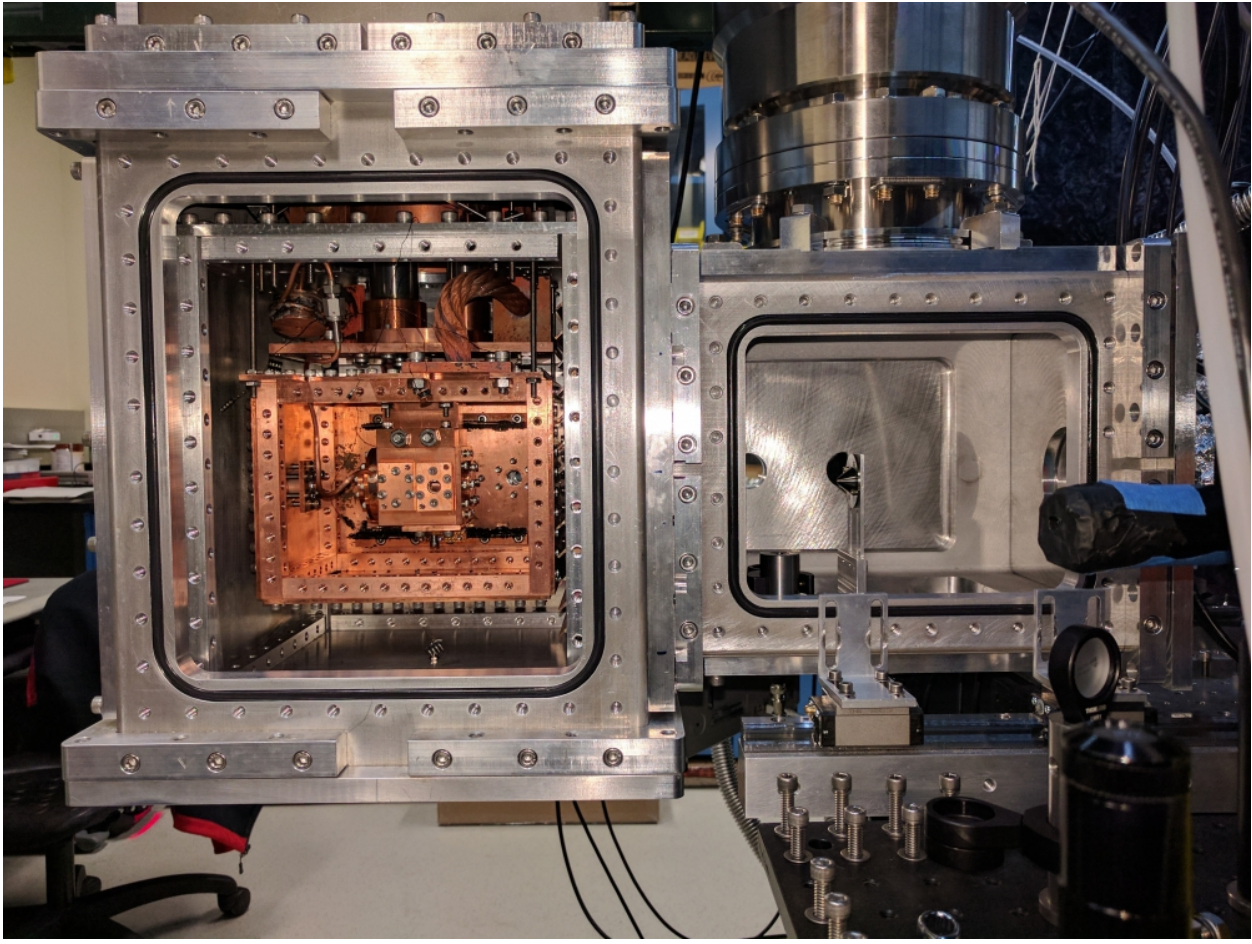


Figure 2.3: Cross sectional view of CBGB with side walls removed from the outer vacuum chamber, 40K aluminum radiation shield, and inner 4K cryopumping shield exposing the inner experimental cell. A skimmer is mounted in the stem region.

### 2.1.1 Heat Load and Thermal Conductivity

To produce a beam of cold particles, various components need to be held within specific temperature ranges to ensure proper operation. Considering neon as the buffer gas species of choice, the experimental cell needs to be maintained at 20K to prevent the neon from freezing to the walls and maintain a high stagnation density that allows for tuning of the flow regime. Conversely, we need the cryopumping shield surrounding the experimental cell

to maintain a temperature  $< 17K$  so that the neon that escapes the cell is readily captured, as the turbo connected to the stem chamber cannot keep up with the gas load. A lack of proper cryopumping results in high densities in the chamber, which scatters the beam.

The PTR 40K cooling stage has 40W of cooling power, while the lowest 4K stage has only 4W. The low cooling power of the lowest stage means that extra care is needed to minimize the heat transfer to the stage from the higher temperature regions including black body radiation and conducted heat from high temperature surfaces.

Material choices used in the CBGB are dictated by their thermal conductivity down to the temperature ranges of interest. At room temperature, thermal conductivity ( $k$ ) of a material is dominated by transfer of energy via phonons through the material. In this regime, different alloys and purities of a material do not greatly affect the conductivity. But once we enter cryogenic temperatures, the conductivity is dominated by electron motion through the material, meaning that purer samples have fewer imperfections to scatter off of, yielding higher conductivities. At these temperatures, it's convenient to characterize the conductivity of a material with the residual resistance ratio ( $RRR = \frac{R(T=295K)}{R(T=4K)}$ ), which can be related to the thermal conductivity with the Wiedemann-Franz Law.[?]

Al 6061 was chosen for the radiation shield for its thermal conductivity ( $k_{Al6061}(T = 40K) = 70\text{W}/(\text{m K})$ [?]), ease of machining, as well as lightweight properties. The thermal mass of the aluminum shield coupled with its relatively lower thermal conductivity (compared to Cu 10100) means the cool down of this region limits the cool down process to 6hr until at workable temperatures. The face of the aluminum shield coinciding with the outgoing buffer gas beam was fitted with a set of stacked chevron baffles as seen in figure 2.2. The baffle design blocks stray light from entering the radiation shield, while enabling gas to pass from the enclosed shields into the stem region, preventing high density regions from forming and scattering the beam. Conversely, the baffles allow for gas within the stem region to reenter the cryogenic shields and facilitate cryopumping of stray particles.

The copper region contains the experimental cell, encompassed by a copper enclosure that acts as a cryopumping surface at the appropriate temperatures. Cu 10100, or oxygen

free copper, was chosen for these components for its high thermal conductivity through to 4K,  $RRR = 2000$ ,  $k_{Cu10100}(4K) = 10^4 \text{W}/(\text{m K})$ [?]. Because it is heat sunk into the same cooling stage as the experimental cell, the copper enclosure does not act as a radiation shield for it does not redirect the heat load away from the experimental cell's cooling surfaces. To maintain a beam, while still cryopumping, the experimental cell is held at a temperature higher than that of the cryopumping shield, the cell is connected to the shield with a SS316 stand off, which has poor thermal conductivity, especially at lower temperatures. A resistive heater and temperature sensor diode (DT-670) are mounted to the cell and controlled with a Lakeshore controller (Model 325) to maintain a set point temperature.

The main heat loads onto the system are those from the black body radiation, as well as the stainless steel rods supporting the shields from the top mounting plate. The heat load and transient solutions over the system may be determined by solving the heat/diffusion equation.

$$\frac{\partial u(x, t)}{\partial t} = D \nabla^2 u(x, t) \quad (2.4)$$

$$\dot{Q} = \frac{A}{l} \int_{T_1}^{T_2} \lambda(T) dT \quad (2.5)$$

$$E = \sigma T^4 \quad (2.6)$$

$$\lambda_{max} T \approx 2900 \mu\text{m K} \quad (2.7)$$

$$\dot{Q} = \sigma A (T_1^4 - T_2^4) \frac{\epsilon_1 \epsilon_2}{\epsilon_1 + \epsilon_2 - \epsilon_1 \epsilon_2} \quad (2.8)$$

### 2.1.2 Gas Fill Lines

To have a functioning beam, we need to introduce both the buffer gas as well as the target species gas from room temperature without over burdening the cooling stage. The buffer gas fill line is made of thin walled SS316, minimizing the thermal connection between the room temperature mounting and the cold experimental cell. It is thermally anchored to the 40K cooling stage and then brazed onto a plate that mounts to the experimental cell. The tubing avoids the copper cryopumping shield as contact will cause local freezing of the gas, resulting in a blocked fill line.

More care must be taken for the design of the water fill line, as it cannot make contact with any cooled metal surface for fear of local freezing. The mating of the fill line to the experimental cell must also prevent excessive heat loads onto the cell while still enclosing the back side. The solution was to utilize a thick walled 1/8" copper tube, with the tip bent at 90°, that enters from the bottom of the CBGB (figure 2.4), through the shields, and enters the back of the experimental cell. The fill line can be manipulated from the bottom of the chamber and the insertion depth into the cell can be adjusted before pump down. By slathering the o-ring at the bottom of the chamber with silicon vacuum grease, one may also adjust the tubing in situ.

Leaving the back of the cell open allowed for minimal heat transfer between the fill line and the cell, but did not allow for a reliable beam. Ice readily formed on the nearby copper surfaces and slowly closed the back opening, decreasing the effective  $A_{aperture}$  of the cell, changing the flow properties. The back was replaced with a 0.001inch film of kapton with a cross cut into the middle for the fill line as seen in figure 2.5. The poor thermal conductivity of kapton (0.5W/(m K)) ensures minimal heat load onto the cell, prevents ice from forming, while also closing the back of the cell. The beam may be run continuously with water entrained in the neon buffer gas for over 10 hours without any change in beam properties.

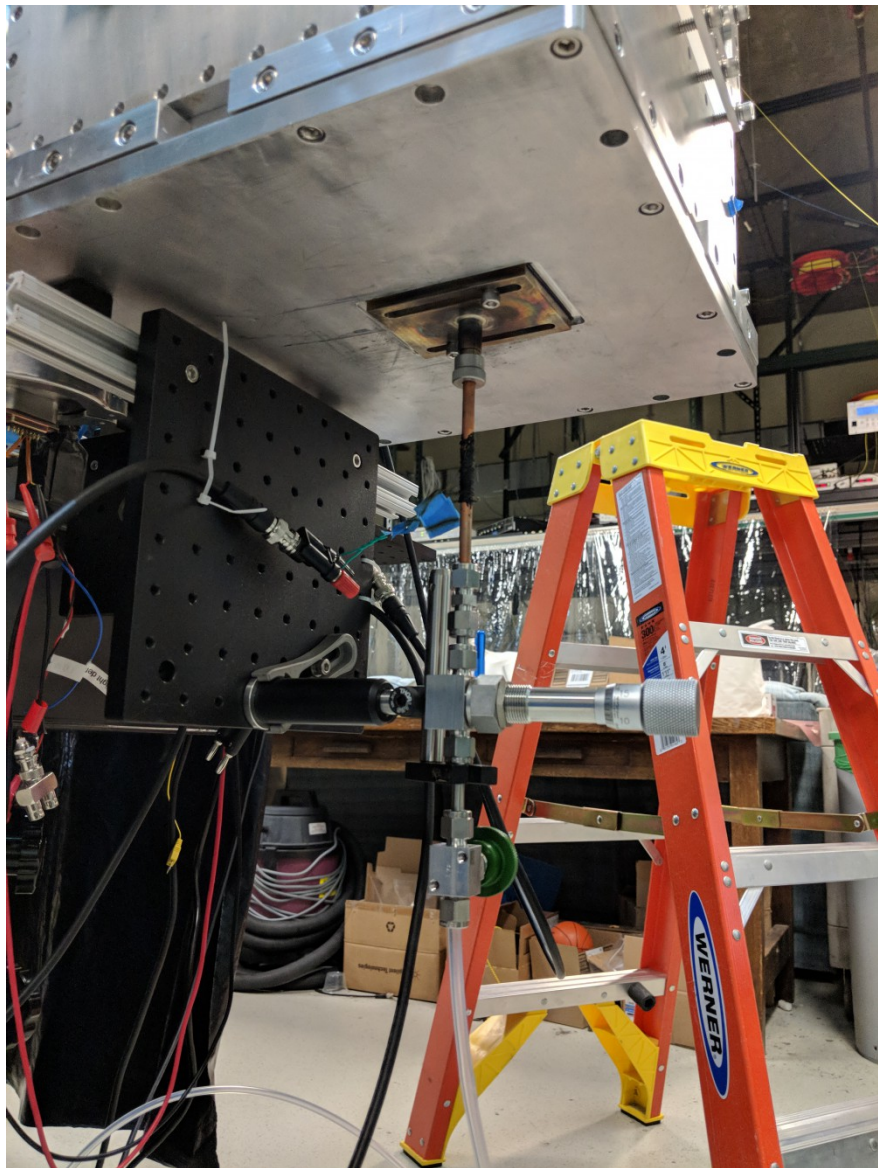


Figure 2.4: The water fill line, sealed by an ultratorr fitting and heated by nichrome wire. A shut off valve and vernier valve are used to regulate the flow of water into the buffer gas cell.

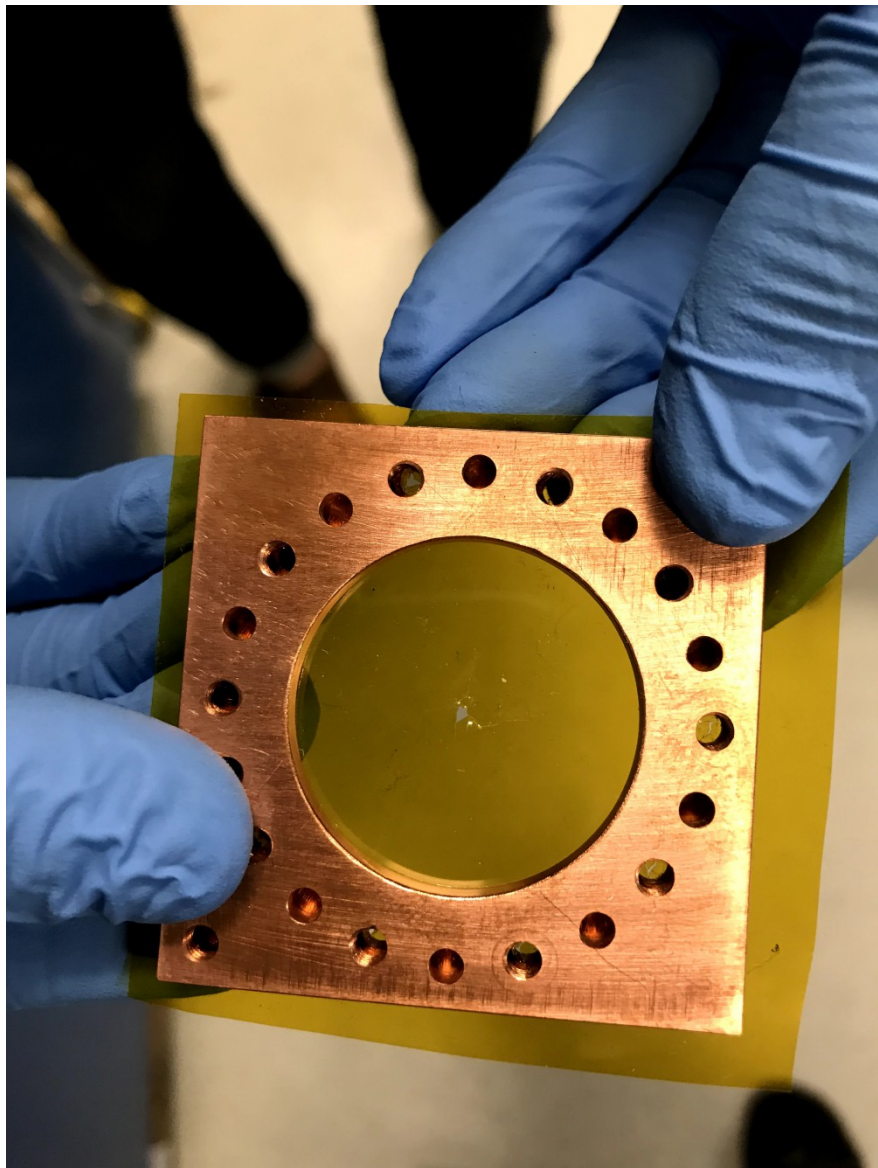


Figure 2.5: A kapton film serves as the back wall of the buffer gas cell with a hole punctured for the insertion of the water fill line. The kapton surface seals the back of the cell for a stronger forward beam, while limiting the heat load from a room temperature fill line, and resisting ice formation allowing for continuous and consistent operation with water for over 10 hours.

## 2.2 Beam Density and Extraction

The stagnation density inside the buffer gas cell is a function of the physical dimensions of the cell and the number flow rate into the cell. High stagnation densities allows for high densities of reactants at the ion trap center, but can push the beam into an unwanted flow regime where the beam properties are not what one wants. Experimentally, it's preferable to use volumetric flow rates when operating the apparatus, but for calculations, that needs to translate to number flow rate using the ideal gas law:

$$\dot{N} = \frac{Pf}{k_B T}$$

where  $P$  is pressure and  $f$  is the volumetric flow rate, this translates to about  $4 \times 10^{17}$  particles/s<sup>-1</sup> for 1SCCM of gas flow. By solving for the number density in the flow out of an aperture with molecular flow, we find that the stagnation density within the cell can be shown as:

$$n_b = \frac{4\dot{N}}{A_{\text{aperture}}\bar{v}} \quad (2.9)$$

In general, buffer gas beams operate with stagnation densities around  $10^{15} - 10^{17}$  cm<sup>-3</sup>. Outside of the cell, we can describe the density of the beam as a function of distance. [33]

$$n(z) = \frac{n_0}{2} \left( 1 - \frac{z}{\sqrt{z^2 + a^2}} \right) \quad (2.10)$$

Where  $z$  is the distance from the aperture into the vacuum side,  $n_0$  is the initial number density,  $a$  is the radius of the aperture. In the far-field, this goes to:

$$n(z) = \frac{n_0 a^2}{4z^2}$$

But there is something that we must consider, that is that we aren't seeing the full aperture while we are at all locations, we are actually seeing an appended area due to the inclusion of apertures and skimmers in the way. So in the calculation for  $n(z)$ , only  $n_0$  has

a dependence on the aperture size of the cell,  $n(z)$  itself will have a set value defined by the smallest aperture in the beam path. For us, although our cell aperture is  $\approx 9\text{mm}$  in diameter, we have multiple apertures and skimmers in the way, of which, a skimmer from Beam Dynamics with a diameter of 2mm is used.

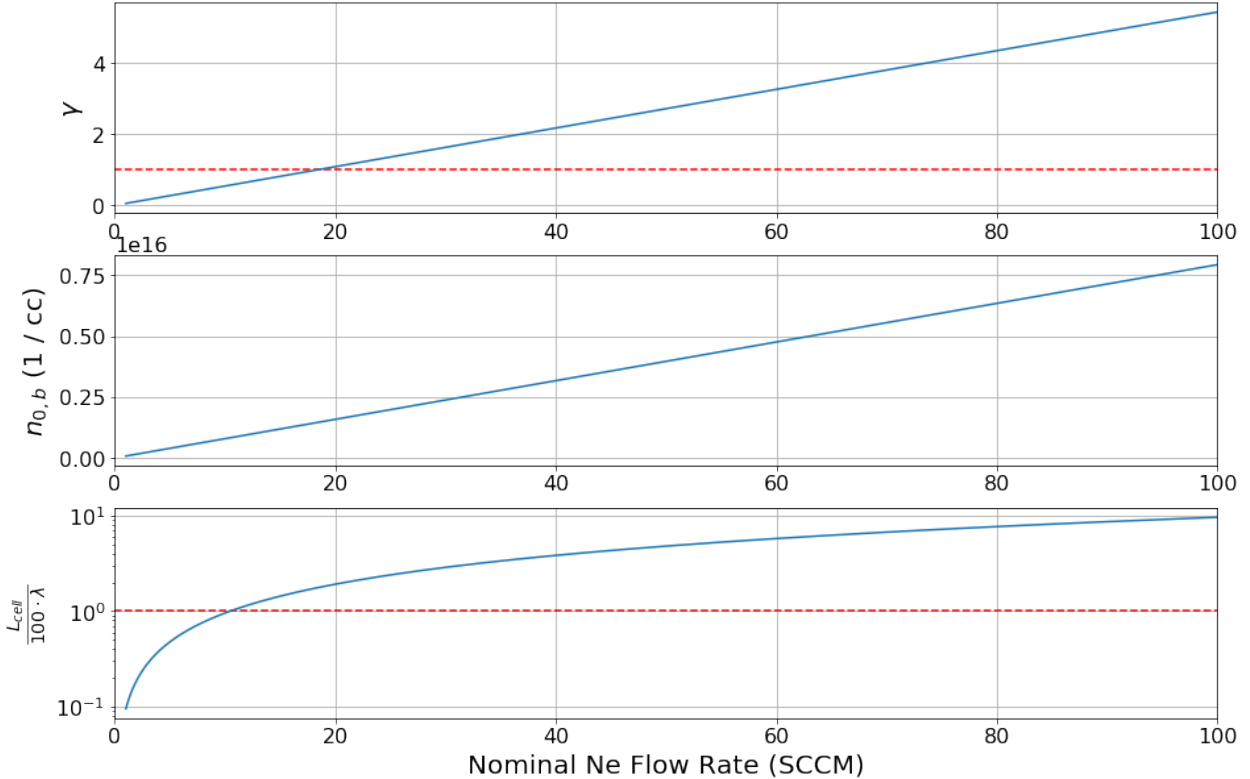


Figure 2.6: A)  $\gamma$  extraction ratio, dotted red line indicates  $\gamma = 1$  where hydrodynamic entrainment begins. B) Theoretical number density of buffer gas species within buffer gas cell. The density of target species introduced should stay under 1% of the buffer gas density. C) Number of collisions a target species particle would expect before extraction out of the cell, the dotted red line indicates 100 collisions before extraction when rotational degrees of freedom are characteristically thermalized.

Sympathetic cooling occurs through collisions between the hot target species being introduced and the cryogenic buffer gas particles. The thermalization of the target species

with the buffer gas particles is derived via momentum conservation of hard sphere collisions, where  $\approx 10$  and  $\approx 100$  collisions are needed to relax translational and rotational states to within a factor of 2 of the buffer gas temperature. Vibrational degrees of freedom may take upwards of  $10^4$  collisions to fully thermalize if the elastic collision energy is much lower than the internal vibrational level. By finding the mean free path, we can consider the characteristic length the particles travel to be thermalized with the buffer gas, this is then compared to the characteristic length of the cell to determine the effectiveness of the cooling.

$$\lambda = \frac{A_{aperture} \bar{v}}{4f\sigma \sqrt{m_s/m_b}}$$

If a species is introduced into the buffer gas cell that has a lower vapor pressure than that is allowed at the current temperature, it will be lost when it comes in contact with the cell walls. The rate of this loss can be described as the characteristic time of diffusion of a particle in the buffer gas to the physical dimensions of the cell set the diffusion time constant:

$$\tau_{diff} = \frac{16}{9\pi} \frac{A_{cell} n_{0,b} \sigma}{\bar{v}} \quad (2.11)$$

where  $\sigma$  represents the collisional cross section for the buffer gas with the target species. On the other hand, we have the characteristic pump out time given by the conductance of a cell aperture:

$$\tau_{pump} = \frac{4V_{cell}}{\bar{v} A_{aperture}} \quad (2.12)$$

By combining equations eqs. (2.11) and (2.12), we can get a dimensionless ratio,  $\gamma$  that characterizes the extraction fraction out of the cell.

$$\gamma = \frac{\tau_{diff}}{\tau_{pump}} = \frac{\sigma f}{L_{cell} \bar{v}} \quad (2.13)$$

Notice that the  $\gamma$  factor does not depend on aperture size, this is generally true, but increasing the aperture size will lower your number density within the cell, which then

influences the characteristic length scale of thermalization. Larger apertures thus run the risk of not allowing your particles to fully thermalize in rotational/vibrational states. But decreasing the aperture size can make alignment as well as controlling the number density more difficult, as finer control over the flow rate is necessary for equivalent flow regimes.

We have utilized a residual gas analyzer (RGA) to determine the density of the beam in the ballistic regime upstream from the ion trap. Inserting the RGA into the beam path allows us to estimate the density of water in the beam as a function of the nominal buffer gas flow rate, as shown in figure 2.7. Using that fit, we find good agreement with the theoretical calculations showing our flow to be near the supersonic regime, while staying in the hydrodynamic regime with a linear extraction efficiency dependence with the flow rate expressed in 2.13.

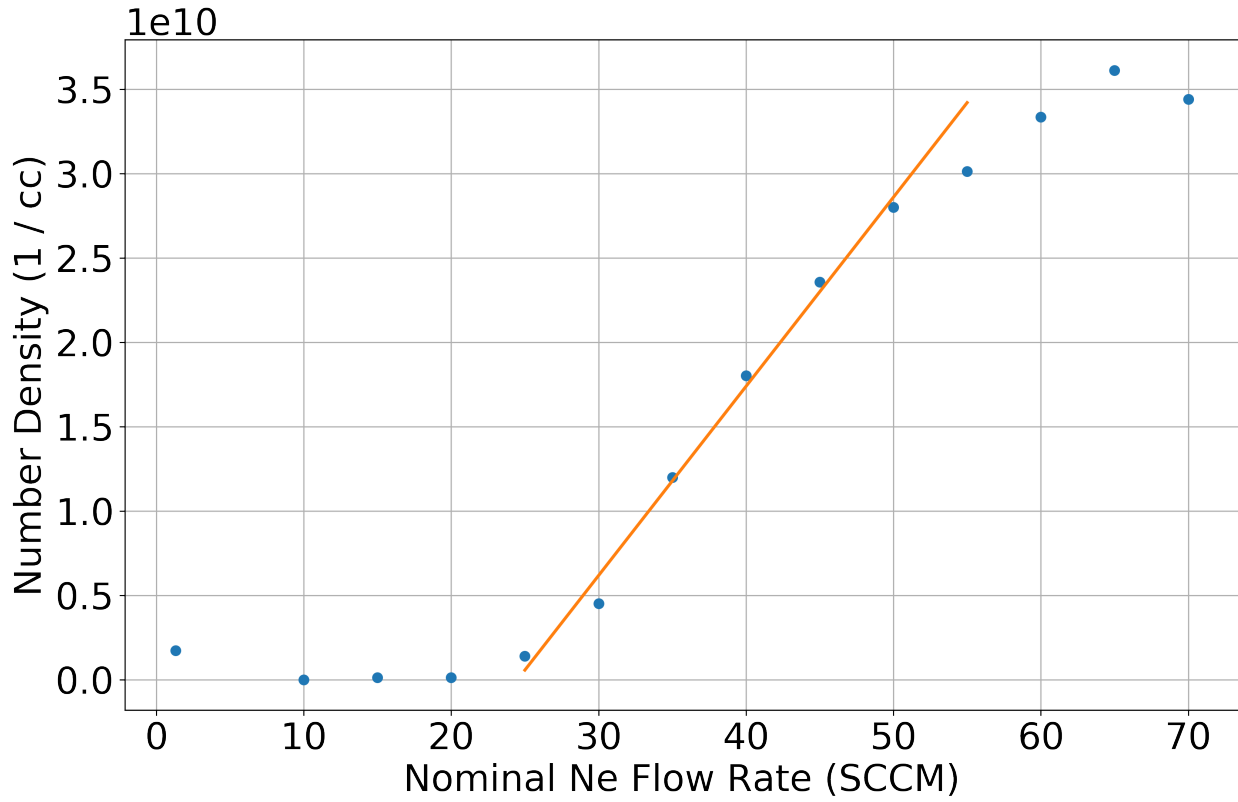


Figure 2.7:  $(1.12 \times 10^9)f - (2.75 \times 10^{10})$

We know have previously calculated the possible number densities of the buffer gas with varying aperture sizes and flow rates. But now we can utilize those equations with the data on the target species to plot out the range of densities that we may see at the trap center as a function of the various apertures that we may utilize. Combining equations eqs. (2.3), (2.9) and (2.10)

But what we really care about is the region in which the number density is linearly dependent to the buffer gas flow rate, not over all possible ranges; we've seen that the target species only behaves linearly once it has been entrained in the buffer gas. This means that we should be equating the density function with the linear fit performed on the data for the parameters the data was taken at,  $n(z) = mf + b$ .

$$\alpha = \frac{m}{\beta} + \frac{b}{\beta f}$$

Where we let  $\beta = \frac{1}{A_{\text{aperture},0}\bar{v}_0} \left( 1 - \frac{z_0}{\sqrt{z_0^2 + a_0^2}} \right)$ . Thus, we may get a final form that incorporates the linear slope's dependence on the other variables of the system as well as the overall experimentally derived scaling factor from the data.

$$n(z) = \frac{mf + b}{A_{\text{aperture}}\bar{v}\beta} \left( 1 - \frac{z}{\sqrt{z^2 + a^2}} \right)$$

There is a mass dependence in the thermal velocity equation, which leads us to conclude that the choice of the species is a statement of the efficacy of the beam itself. If we choose to calculate the thermal velocity of the target species found in the beam due to the theoretical thermal velocity of the buffer gas, that indicates that the beam properties are still dominated by the buffer gas species. This may not be the case, as we see in our data, we have a ratio of about 10:1, this is pushing the boundaries of the assumption that the buffer gas far outnumbers the target species. At these ratios, we may start to see the effects of the target species on the beam properties.

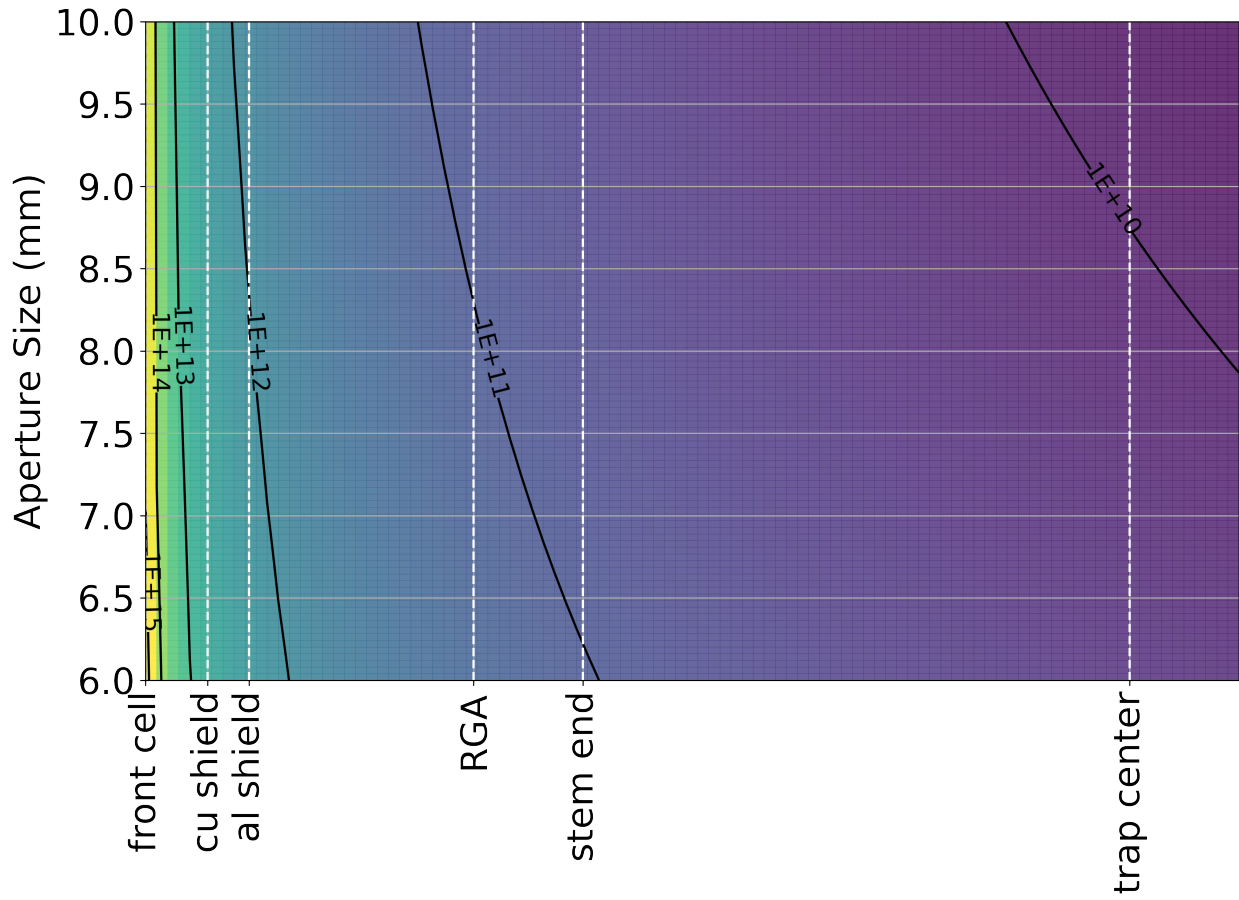


Figure 2.8: Projected buffer gas beam densities with a Ne flow rate of 30SCCM with various distances of interest within the chamber. Optimal densities of entrained gasses hover around 0.1% of the buffer gas value shown here.

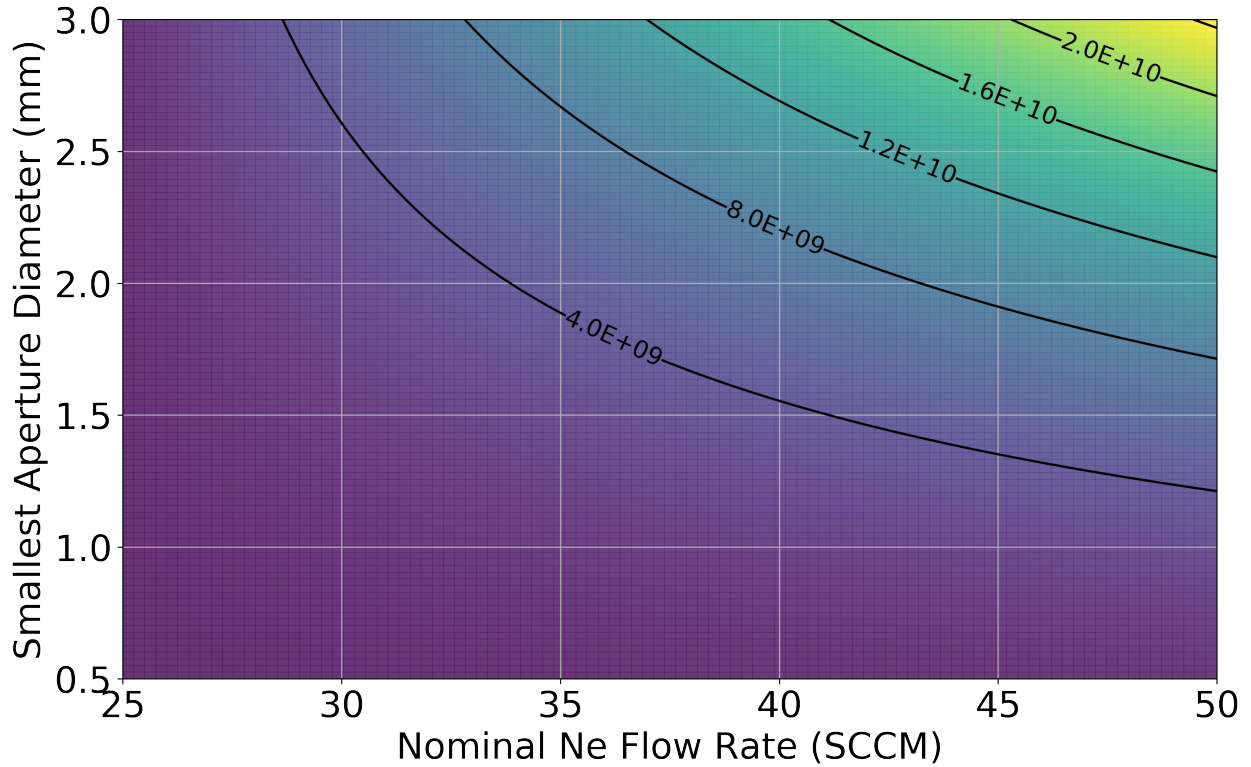


Figure 2.9:

Extrapolating the fit and estimated density from figure 2.7, we can estimate the density of the water at various locations along the beam line as shown in figure 2.8. We find that we should be able to produce an appreciable number density of water down at the trap center.

From the RGA, we were able to open and close a shutter in the beam path and see an extinction of the water signal, but a more accurate representation would be from the ions in the trap themselves. We know that the trapped  $\text{Be}^+$  ions will react with  $\text{H}_2\text{O}$  to predominately produce  $\text{BeOH}^+$ , which we see as a drop in the fluorescence. Figure 2.2 shows fits of the fluorescence decay as a beam from the CBGB is suddenly blocked by our shutter in the beam line. Comparing the fitted reaction rates, we find that they agree with the background rates found as shown in figure 2.2. This indicates to us that we indeed have a beam of cryogenic water coming from the CBGB, as seen by the sudden extinction of the  $\text{Be}^+ + \text{H}_2\text{O}$  reaction.

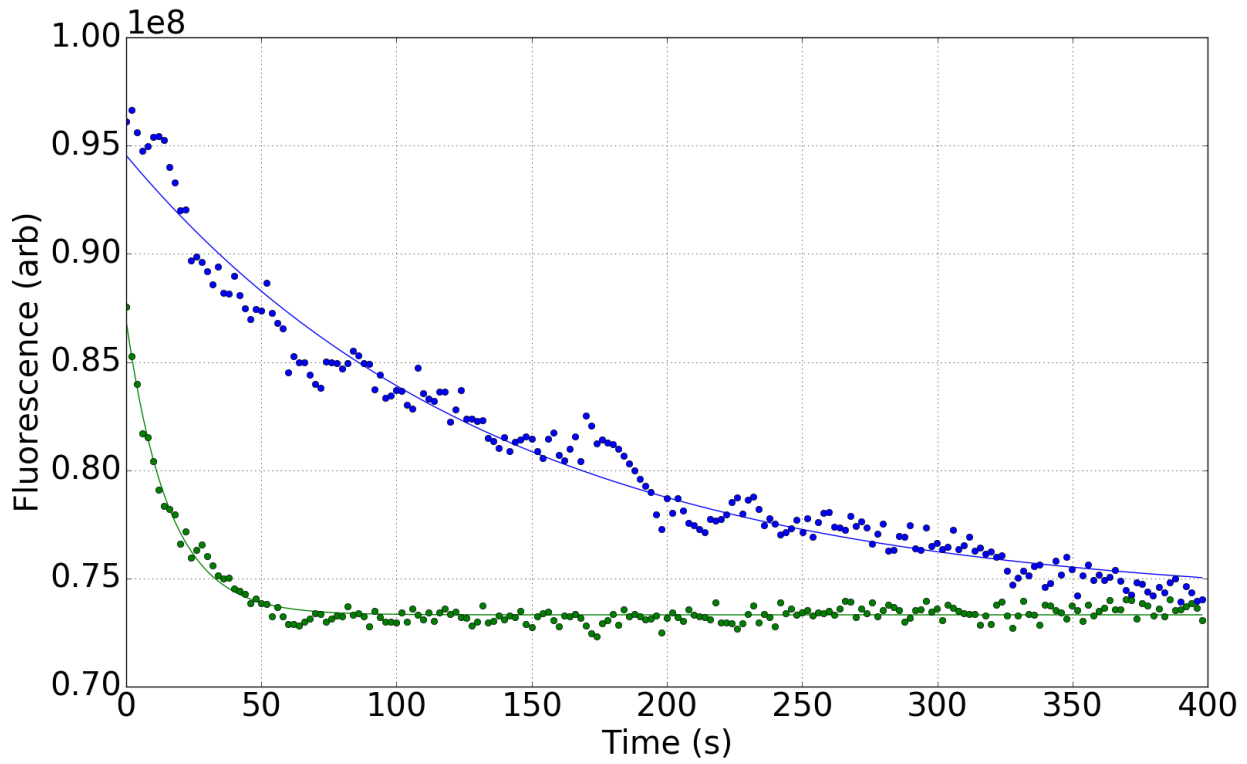


Figure 2.10: Fluorescence decays of loaded  $\text{Be}^+$  ions exposed to a cold water beam with an inline shutter either opened, in green ( $\tau = 7.23 \times 10^{-3}\text{s}$ ) or closed, in blue ( $\tau = 6.37 \times 10^{-2}\text{s}$ )

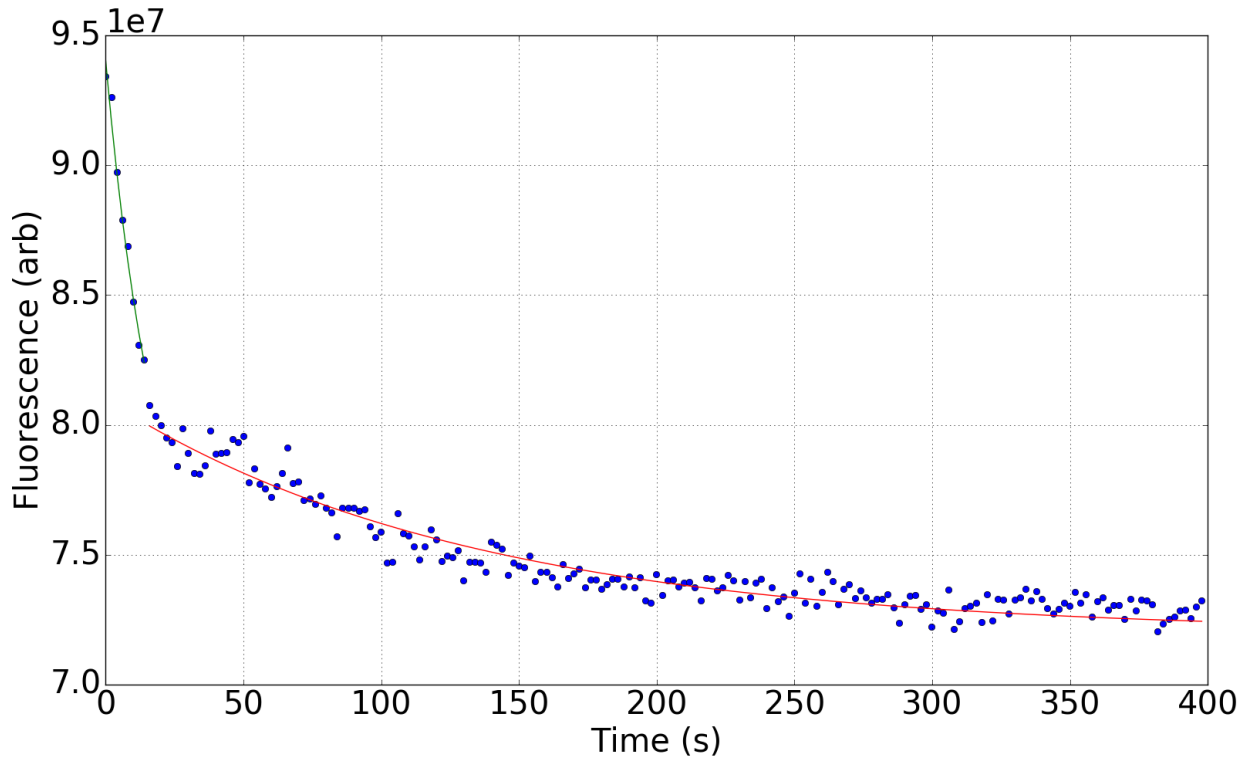


Figure 2.11: Fluorescence decays of loaded  $\text{Be}^+$  ions exposed to a cold water beam with an inline shutter opened, in green ( $\tau = 5.37 \times 10^{-2}\text{s}$ ) or closed, in red ( $\tau = 7.59 \times 10^{-3}\text{s}$ )

### 2.3 Beam Velocity

We may rewrite the equation 2.2 as a function of the mean velocity  $\bar{v}$  into a simpler form .

$$f(v) = \frac{32}{\pi^2} \frac{v^2}{\bar{v}^3} e^{-4v^2/\pi\bar{v}^2} \quad (2.14)$$

To get the velocity distribution in the beam, we can calculate the distribution of particles incident on an aperture in the cell.

$$\begin{aligned} f_{beam}(v) &= \frac{v}{\bar{v}} f(v) \\ &= \frac{32}{\pi^2} \frac{v^3}{\bar{v}^4} e^{-4v^2/\pi\bar{v}^2} \end{aligned}$$

For low Reynold's numbers ( $Re < 1$ ) the flow at the aperture is purely molecular, which means that there are few to no collisions. This allows us to continue to use the Maxwell-Boltzmann distribution to describe the forward velocity [23].

$$\bar{v}_{\parallel} = \int_0^{\infty} v f(v) dv \approx 1.2\bar{v} \quad (2.15)$$

The spread of the forward velocity of an effusive beam is the full width half max (FWHM) of the Maxwell-Boltzmann distribution:  $\Delta\bar{v} \approx 1.5\bar{v}$ . As the Reynolds number increases, one can reach the supersonic regime ( $Re > 100$ ) where the forward velocity reaches  $1.4\bar{v}$  and the distribution drastically narrows.[23, 33]

But as the flow regime nears the supersonic regime, forward collisions around the aperture cause boosting of the average velocity as well as a decrease in the velocity spread. Changing the flow regime may also change the ratio of species in the beam as well.

A helium buffer gas held at 4K will have a slower forward velocity than that of a neon gas held at 17K. Despite this, it is preferable to use neon as a buffer gas due to its ideal cryopumping properties. Helium requires large amounts of activated charcoal, also held at low temperatures, to effectively cryopump. These volumes of charcoal can then become saturated and require purging, limiting one's operating time (few hours). Neon on the other hand, only requires a metal surface lower than 17K to create neon ice. The neon ice surface will then act as a cryopump for more neon gas as well, allowing for many hours of continuous operation with no appreciable build up of background gas. Our experiment uses neon as a buffer gas for its technical simplicity, the lower achievable temperature with the helium does not yield dramatic gains in the final reaction temperature.

To better understand the reaction temperatures we will be able to reach, we need a characterization of the beam's velocity, more specifically, the velocity of the target species

entrained within the buffer gas. By ablating ytterbium into the neon buffer gas, we find that the ytterbium is entrained within the neon and sympathetically cooled to the cell's temperature. As long as the target species number density is a trace amount in comparison to the bulk buffer gas number density (0.1%), the flow characteristics are dominated by the buffer gas species [22]. The forward velocity of the beam is not only parameterized by the temperature of the buffer gas species, it is also dependent on the flow regime. As we increase the flow of neon into the cell, figure 2.7 shows a linear increase in the H<sub>2</sub>O signal from a downstream RGA. This coincides with the beam operating within the intermediate flow regime, where there are few collisions at the cell aperture, resulting in a slight forward boosting and increased extraction efficiency of the target species. At higher flow regimes, entering the supersonic regime, we would see a "freeze out" where the forward velocity reaches  $1.4\bar{v}$  and we would not see appreciable gains in species extraction [22]. We chose to operate at a nominal neon flow rate of 30SCCM based upon the reaction rate of the ions downstream.

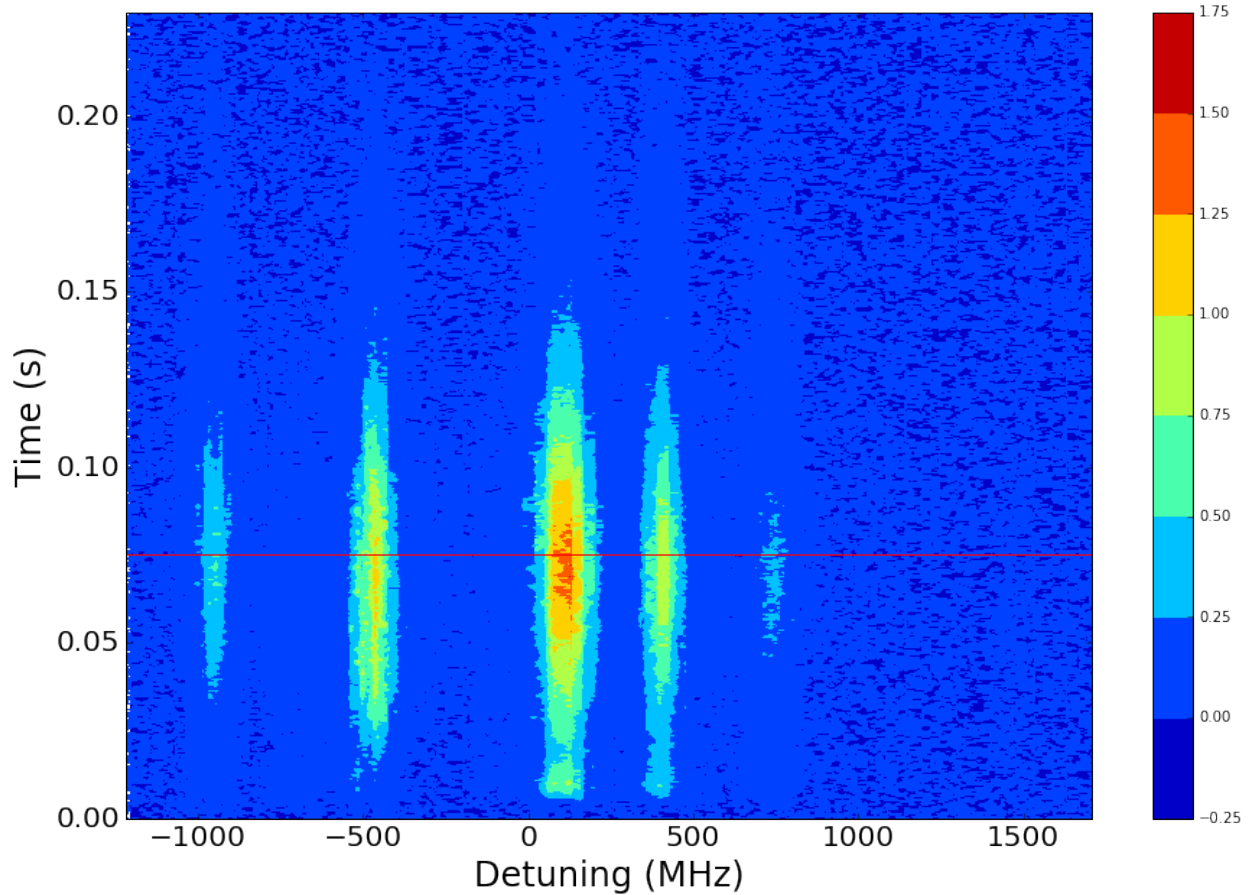


Figure 2.12:

find  
ap-  
pro-  
pri-  
ate  
plot

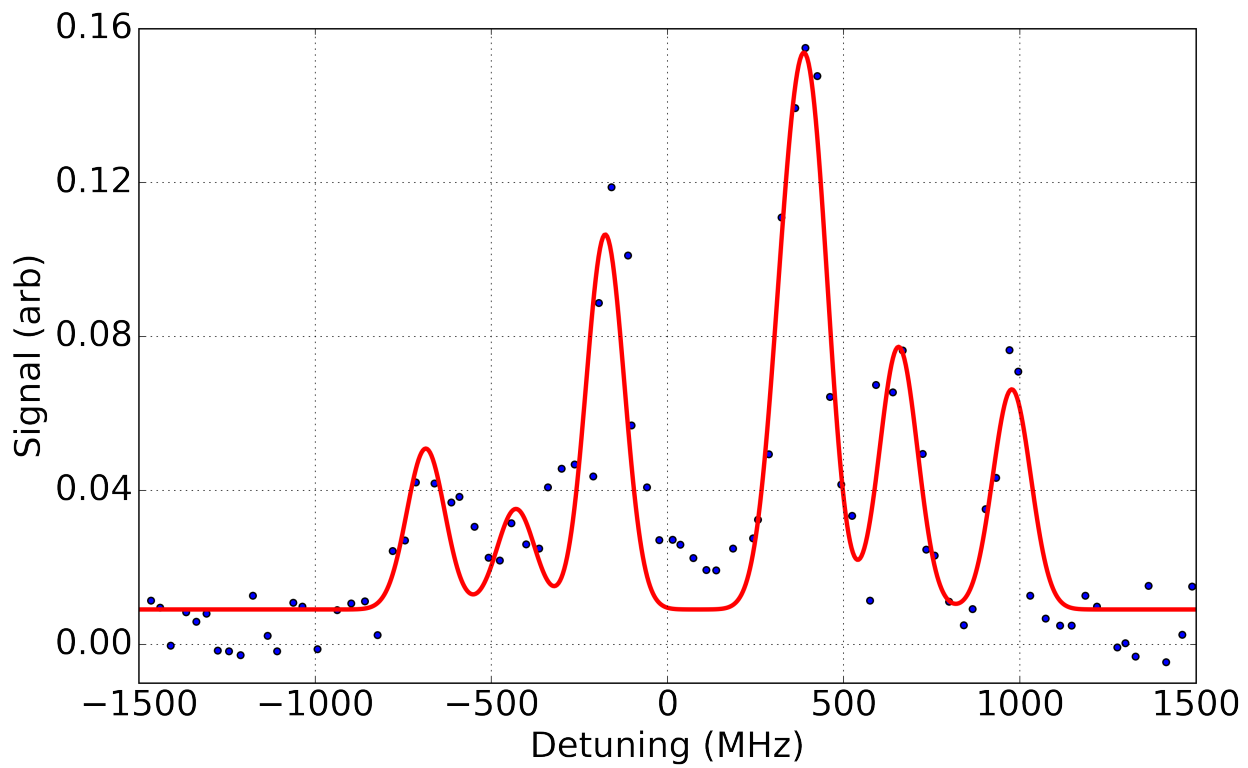


Figure 2.13:

# CHAPTER 3

## Trapping and Cooling Ions

### 3.1 Ion Trapping

### 3.2 Vacuum Requirements

To reliably laser cool and trap ions into crystals, it is ideal to have ultra-high vacuum (UHV) which is generally defined as having a pressure  $< 10^{-9}$  Torr. The characteristic collision rate between a monopole and polarizable neutral is defined by the  $C_4/r^4$  attractive term. By considering the Langevin collision rate constant

### 3.3 ${}^9\text{Be}^+$ Laser Cooling

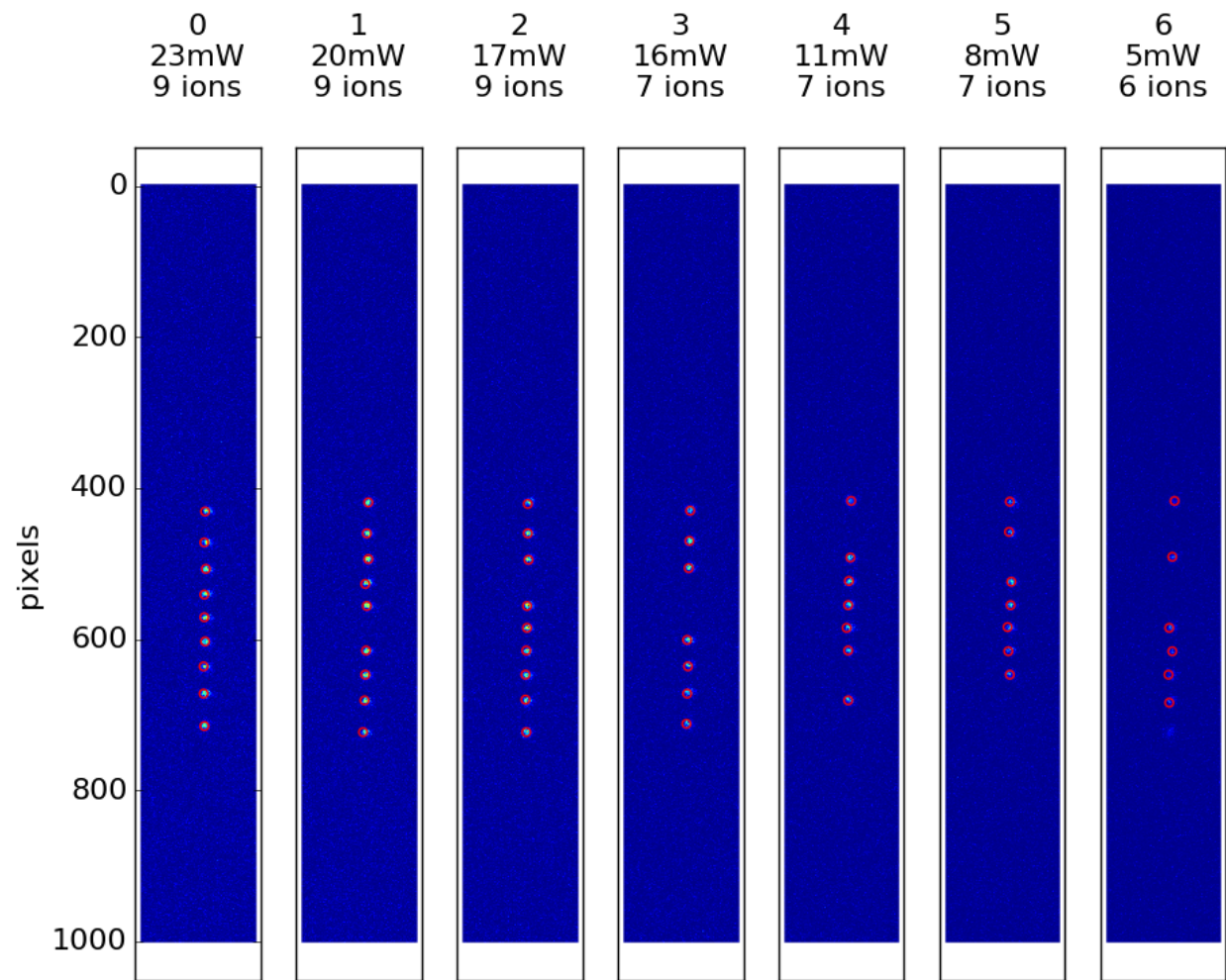


Figure 3.1: Set of ion images taken at various 313nm powers with an algorithm that identifies individual ions

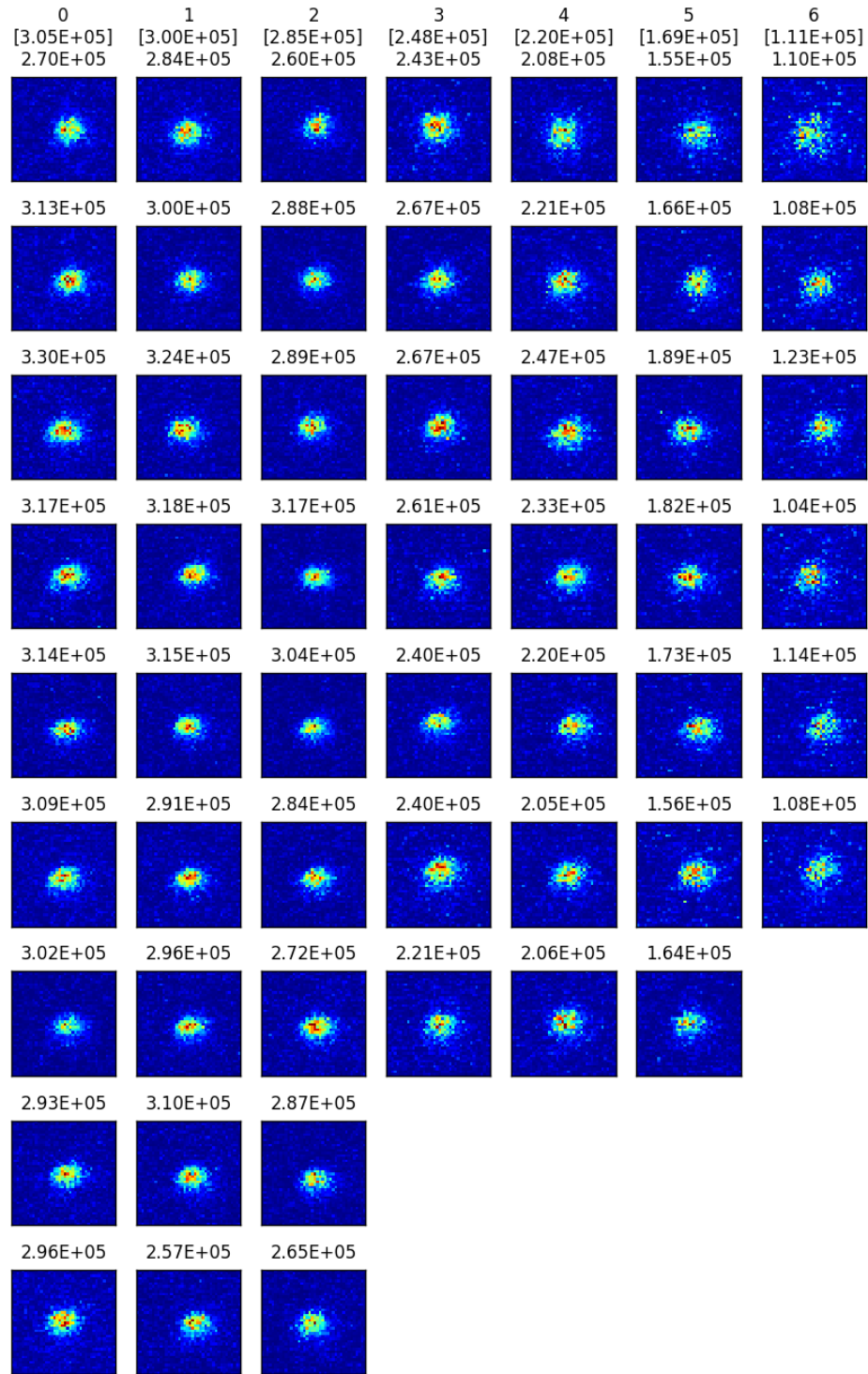


Figure 3.2: Individual ions identified from images in figure 3.1. Integrated fluorescence counts shown for each image as well as averaged value in brackets.

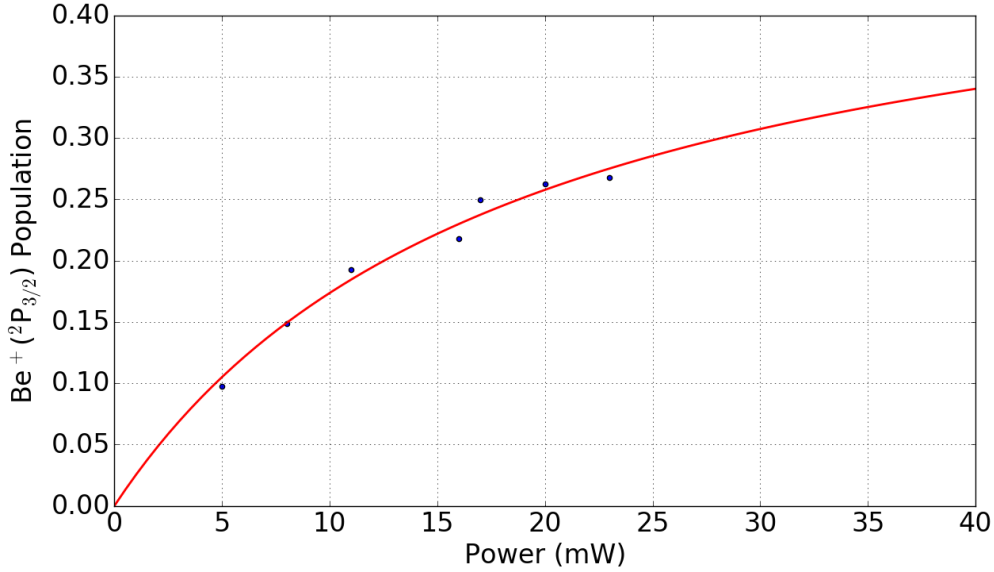


Figure 3.3: P-state fraction curve fitted to incident laser power at a fixed detuning of  $\omega_l = \omega_0 - \Gamma/2$ .

### 3.4 Time of Flight Mass Spectrometer (TOF-MS)

pew pew shoot the ions into a tube and measure their mass

### 3.5 Dual Species Loading

Although loading and cooling  $\text{Be}^+$  ions is fairly straight forward, it is not as clear as how to load  $\text{C}^+$  ions into the trap with  $\text{Be}^+$  reliably. Early attempts involved using the home-made electron gun to electron dissociate and CO gas introduced via leak valve, all possible ionized products of CO were detected ( $\text{C}^+$ ,  $\text{O}^+$ , and CO). Even when loading into an empty trap, it was not possible to reliably isolate the  $\text{C}^+$  via A-ramping of the trap RF voltage. Prolonged use of the electron gun directly towards the ion trap also caused charging that would slowly dissipate and change the trap parameters. On top of these complications, it would have to work in conjunction with ablation loading  $\text{Be}^+$ .

Instead of using two different methods to load the different ion species, ablating both

simultaneously was found to be the best method. A sample of Be metal was placed on top of a piece of graphite on the target holder so that both samples were in view of the ablation laser. The set up shown in figure 3.4 allowed us to separate the ablation laser into two beam with independent alignment and focal planes. The polarization of the laser light is rotated with a half-waveplate, which then enters a polarizing beam splitter (PBS), allowing for tuning of power into either path. The vertically polarized reflected light is reflected again with another PBS and is steered up to the objective lens and then focused into the chamber. The horizontally polarized light transmitted through the first PBS is aligned through an adjustable telescope system. This light is then realigned with the vertically polarized light on the second PBS, co-propagating into the chamber. The "delay stage" for the horizontal light allows for independent focusing and alignment onto the sample.

draw  
on  
fig-  
ure

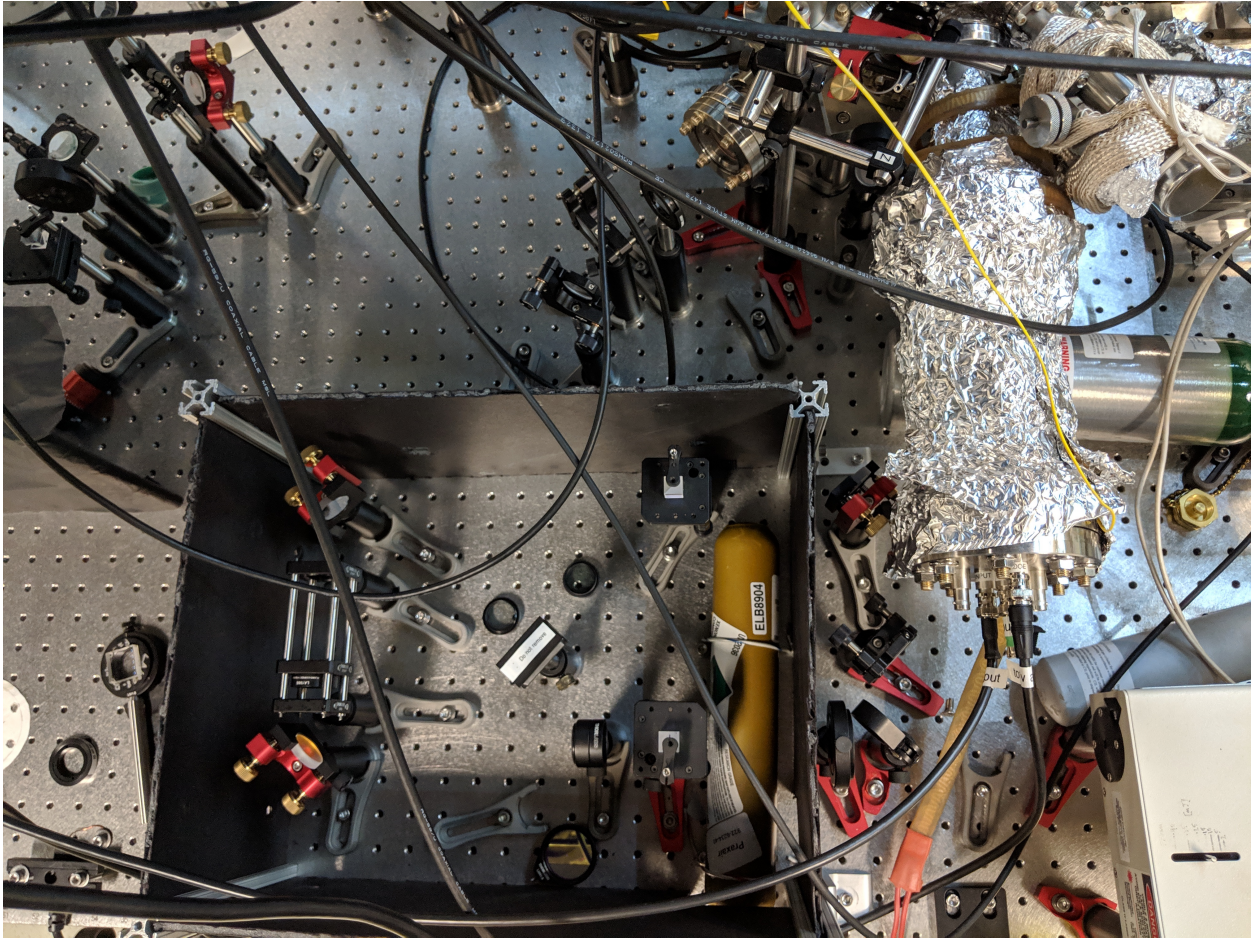


Figure 3.4: Dual ablation set up.

Blocking one beam allowed for adjustments for the ablation of each species independently. When loading  $\text{C}^+$ , we found a strong dependence of the trapped species and the fluence. Lower fluence created not only  $\text{C}^+$ , but clusters of,  $\text{C}_2^+$ , and  $\text{C}_3^+$  as well. Tight focusing of the beam improves the efficiency of creating only  $\text{C}^+$ , but some  $\text{Cn}^+$  is still usually produced, which can then be ejected out of the trap with a soft A-ramp.

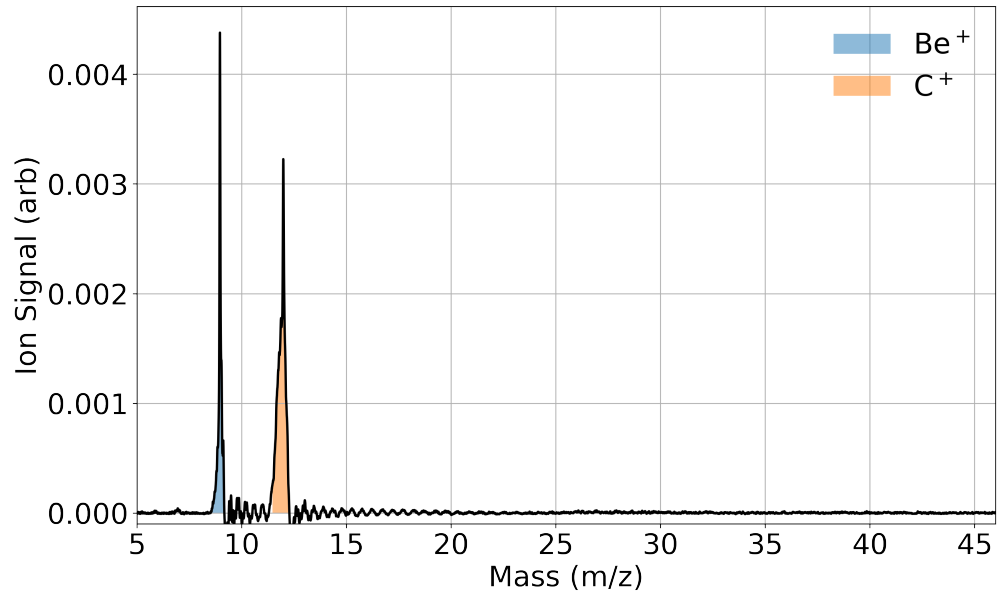


Figure 3.5: TOF trace of simultaneous Be and C ablation averaged over 10 shots. A soft A-ramp is applied after loading, ejecting any unintentionally loaded  $\text{C}_n$  clusters.

## CHAPTER 4

### Pseudo-First Order Reaction

The reactions we are looking at are pseudo first-order, meaning they are mathematically similar to a first order rate, while requiring two reactants.

# CHAPTER 5



## 5.1 Optical Control of Reactions between Water and Laser-Cooled $\text{Be}^+$ Ions

### 5.1.1 Abstract

We investigate reactions between laser-cooled  $\text{Be}^+$  ions and room-temperature water molecules using an integrated ion trap and high-resolution time-of-flight mass spectrometer. This system allows simultaneous measurement of individual reaction rates that are resolved by reaction product. The rate coefficient of the  $\text{Be}^+(\text{^2S}_{1/2}) + \text{H}_2\text{O} \longrightarrow \text{BeOH}^+ + \text{H}$  reaction is measured for the first time and is found to be approximately two times smaller than predicted by an ion-dipole capture model. Zero-point-corrected quasi-classical trajectory calculations on a highly accurate potential energy surface for the ground electronic state reveal that the reaction is capture-dominated, but a submerged barrier in the product channel lowers the reactivity. Furthermore, laser excitation of the ions from the  $\text{^2S}_{1/2}$  ground state to the  $\text{^2P}_{3/2}$  state opens new reaction channels, and we report the rate and branching ratio of the  $\text{Be}^+(\text{^2P}_{3/2}) + \text{H}_2\text{O} \longrightarrow \text{BeOH} + \text{H}$  and  $\text{H}_2\text{O} + \text{Be}$  reactions. The excited-state reactions are nonadiabatic in nature.

#### 5.1.1.1 Introduction

Low-temperature reactions of simple ions with small molecules play a central role in astrochemical environments from interstellar clouds to cometary comae to planetary atmospheres, including that of Earth[2, 24]. The chemical evolution of interstellar molecular

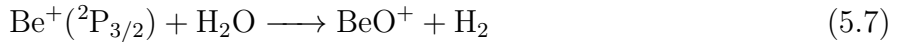
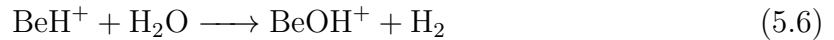
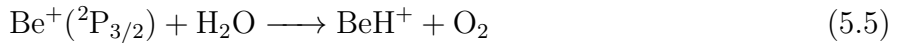
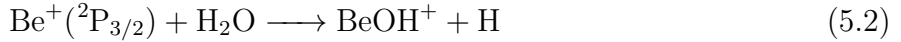
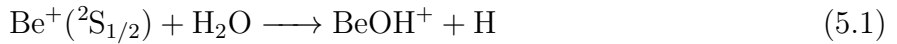
clouds ultimately yields the seedbed from which new stars and planets are born and the raw materials from which life likely developed. A firm understanding of the reaction rates for a host of elementary ion-molecule reactions is essential to accurately model these environments these environments. Techniques such as selected ion flow tubes (SIFTs)[1], guided ion beams[3], and supersonic flows (CRESU)[40] have improved our empirical understanding of these processes; however, each has its own limitations.[43, 44] Theoretically, it has long been recognized that these ion-molecule reactions are often barrierless, and their rates are frequently described by capture models.[16] However, recent studies have revealed that dynamical features can sometimes prevail,[29, 26, 6] in which case statistical treatments may not be accurate.[18, 9] Therefore, new experimental and theoretical efforts are needed to accurately address ion-molecule chemistry.

We have developed an approach, adapted from the ultracold ion community,[20, 50, 53] to study reactions of atomic ions with small molecules. Here we report the use of this approach to study the reaction of  $\text{Be}^+$  with gas-phase water for the first time. There have been very few experimental studies of gas-phase reactions between metal ions and water, especially at low temperature, despite their importance for metal ion chemistry in a range of environments.[19, 32, 52]

Singly ionized beryllium is a particularly attractive metallic reactant to use for such studies because it is both theoretically tractable and experimentally highly controllable. The relatively simple electronic structure of this three-electron ion allows both highly accurate characterization of its electronic structure and laser cooling,[4] and the low mass of  $\text{Be}^+$  lends itself to high motional frequencies as well as efficient sympathetic cooling of other chemically interesting atomic ions when employed in ion traps.[7, 36, 25, 39] For the molecular reaction partner,  $\text{H}_2\text{O}$  is arguably the most important molecule in chemistry, and theoretical studies of its reactions with a single atom have been reported on full-dimensional potential energy surfaces (PESs).[27, 45, 35, 28, 56] Thus this system of reagents provides an opportunity to perform a high-resolution comparison between experiments and theory for a molecule-ion system.

The apparatus employed here is shown in the Supporting Information (SI) (Figure S1). Laser ablation of metallic Be is used to produce  $\text{Be}^+$  ions, which are trapped in a linear radio frequency Paul trap.[55] Laser cooling [54] is used to cool the translational motion of the ions, resulting in a Coulomb crystal of  $\text{Be}^+$  ions. Gaseous, room-temperature  $\text{H}_2\text{O}$  molecules are then introduced via a leak valve into the trapping region, where they react with the trapped ions. Charged products of the chemical reaction remain in the trap and are subsequently detected via an integrated time-of-flight mass spectrometer (TOFMS) recently developed by our group[38, 37] and used to discover new species.[34] The total reaction rate is measured by monitoring the decay of  $\text{Be}^+$  ion fluorescence, and the product branching ratios are extracted from the mass spectrum.

A key feature of this experiment is that by varying the detuning of the 313 nm laser used to cool the ions, the population in the excited  $1\text{s}^2 2\text{p}^1 {}^2\text{P}_{3/2}$  and ground  $1\text{s}^2 2\text{s}^1 {}^2\text{S}_{1/2}$  states can be controlled. Because the energy difference between the ground and excited states is 3.96 eV, several more product channels are open for the  $\text{Be}^+({}^2\text{P}_{3/2}) + \text{H}_2\text{O}$  entrance channel. Using this system, we are able to measure the reaction rate and product branching ratio for these two entrance channels. We find that the ground-state channel,  $\text{Be}^+({}^2\text{P}_{3/2}) + \text{H}_2\text{O}$ , exclusively produces  $\text{BeOH}^+ + \text{H}$ , whereas the excited-state channel,  $\text{Be}^+({}^2\text{P}_{3/2}) + \text{H}_2\text{O}$ , also produces  $\text{H}_2\text{O}^+ + \text{Be}$  with a yield of 10%. Specifically, the reactions considered here are



Because the translational energy of the laser-cooled  $\text{Be}^+$  ions is  $< 0.5$  K, the energy of the room-temperature water sets the reaction kinetic energy of  $\text{Be}^+ + \text{H}_2\text{O}$  in the center of mass frame to 100K. The internal state distribution of the  $\text{H}_2\text{O}$  is assumed to be given by the 300 K. Typical TOF traces (10 sample average) at reaction times  $t = 0$  and 70 s with 7 and 26% relative  $\text{Be}^+(\text{P}_{3/2})$  state excitation are shown in Figure 1A,B, respectively. The fluorescence signal, which is used to determine the reaction time zero and normalize the initial ion number for the TOF, is monitored by the camera (ANDOR iXON3 EMCCD) in real time. At  $t = 0$  s, a large peak of  $m/z = 9(\text{Be}^+)$  and a smaller one of  $m/z = 9(\text{BeOH}^+)$  are evidenced in the TOF trace (blue line), which indicates that  $\text{Be}^+$  ions are the main species in the trap at  $t = 0$ . The finite amount of  $\text{BeOH}^+$  at  $t = 0$  reflects the fact that reactions eqs. (5.1) to (5.8) happen even during the loading process and that the mass filtering procedure is imperfect. At  $t = 70$  s, a  $m/z = 19$  peak emerges when more  $\text{Be}^+$  ions are excited to  $\text{P}_{3/2}$  state, which we identify as  $\text{H}_3\text{O}^+$  resulting from reactions eqs. (5.3) and (5.4). The  $\text{BeOH}^+ / \text{H}_3\text{O}^+$  ratio,  $\eta(P_{\text{P}})$ , is measured by integrating both peaks for the experimentally controlled excited-state population  $P_{\text{P}}$ . The  $\text{BeOH}^+$  signal includes the amount unfiltered during loading, products from both reactions eqs. (5.1) and (5.2), as well as, in principle, the two-step reactions eqs. (5.5) to (5.8). The  $\text{H}_3\text{O}^+$  signal is produced via the two-step reactions eqs. (5.3) and (5.4). Whereas we do not observe products from reactions eqs. (5.5) to (5.8) (see also in SI), they are thermochemically allowed and therefore included in our analysis, which sets upper limits on their reaction rate coefficients.

The total reaction rate is given by  $\Gamma_t = \rho_{\text{H}_2\text{O}} k_t$ , where  $\rho_{\text{H}_2\text{O}}$  is the  $\text{H}_2\text{O}$  density measured from a Stanford Research Systems residual gas analyzer (RGA) calibrated to an ion gauge (see the SI for more information) and  $k_t$  is approximated as  $k_t = P_{\text{S}}k_1 + P_{\text{P}}k_2 + P_{\text{P}}k_3$ , where  $P_{\text{S}}$  and  $P_{\text{P}}$  are the  $\text{Be}^+$  population in the  $\text{S}_{1/2}$  and  $\text{P}_{3/2}$  states, respectively, and  $k_i$  is the reaction rate coefficient of reaction  $i$ . Reaction eq. (5.4) has been studied by other groups, reporting a rate coefficient of  $(2.05 \pm 0.010) \times 10^{-9} \text{ cm}^3/\text{s}$ .<sup>[21]</sup> The measured  $\text{H}_3\text{O}^+ / \text{BeOH}^+$

ratio is given from the reaction rates by

$$\eta(P_{\text{P}}) = \frac{P_{\text{P}}k_3}{P_{\text{S}}k_1 + P_{\text{P}}k_2} \quad (5.9)$$

To use equation 5.9 to extract the individual rate coefficients ( $k_i$ ), the total reaction rate  $\Gamma_t$  is first measured by monitoring the  $\text{Be}^+$  fluorescence decay with a camera, as shown in Figure (see also the SI). Fluorescence decay is monitored directly after a DC voltage applied to trap electrodes is used to filter out the heavier products from the trap to allow better crystallization of the  $\text{Be}^+$  ions by reducing ion-ion heating.[8] The inset of Figure shows typical fluorescence images of the  $\text{Be}^+$  crystal at various times. Fluorescence is used to measure the total reaction rate because the total measurement time is 30 times shorter than using the TOFMS (Figure ). To determine the separate rate coefficients for the  $\text{Be}^+$  ground and excited states, we measure the total reaction rate coefficients for different excited-state fractions, shown in Figure . A linear fit (blue line) is found using the least-squares method. The vertical intercept of this fit gives the  $\text{Be}^+$  ground-state reaction rate coefficient  $k_1 = (2.2 \pm 0.3_{\text{stat}}) \times 10^{-9} \text{ cm}^3/\text{s}$ , whereas the sum of the slope and intercept gives the total excited-state  $\text{Be}^+$  reaction rate coefficients  $k_2 + k_3 = (4.7 \pm 1.7_{\text{stat}}) \times 10^{-9} \text{ cm}^{-3}/\text{s}$ . Using equation 5.9, the reaction rate coefficients of reactions eqs. (5.2) and (5.3) are then calculated to be  $k_2 = (4.2 \pm 1.6_{\text{stat}}) \times 10^{-9} \text{ cm}^{-3}/\text{s}$  and  $k_3 = (0.47 \pm 0.11_{\text{stat}}) \times 10^{-9} \text{ cm}^{-3}/\text{s}$ , respectively. The ratio of reaction rate coefficients for reactions eq. (5.3) to eq. (5.2) is therefore  $k_3/k_2 = 0.11 \pm 0.03$  independent of systematic errors in the density measurement. Charged products from reactions eqs. (5.5) and (5.7) to be  $< 5 \times 10^{-10} \text{ cm}^3/\text{s}$ . Reactions at these upper bounds for the rate coefficients do not significantly change the analysis above, justifying their exclusion from  $k_i$ .

It is instructive to compare these measured rate coefficients to those predicted by capture theory. For an ion reacting with a polar molecule, the leading order interaction potential as a function of the molecule-ion separation  $r$  is described by monopole-dipole interaction ( $U \propto r^{-2}$ ) and the polarization of the molecule by the ion ( $U \propto r^{-4}$ ). For this case, the rate coefficient is typically found using the average dipole orientation (ADO) collision model,[47]

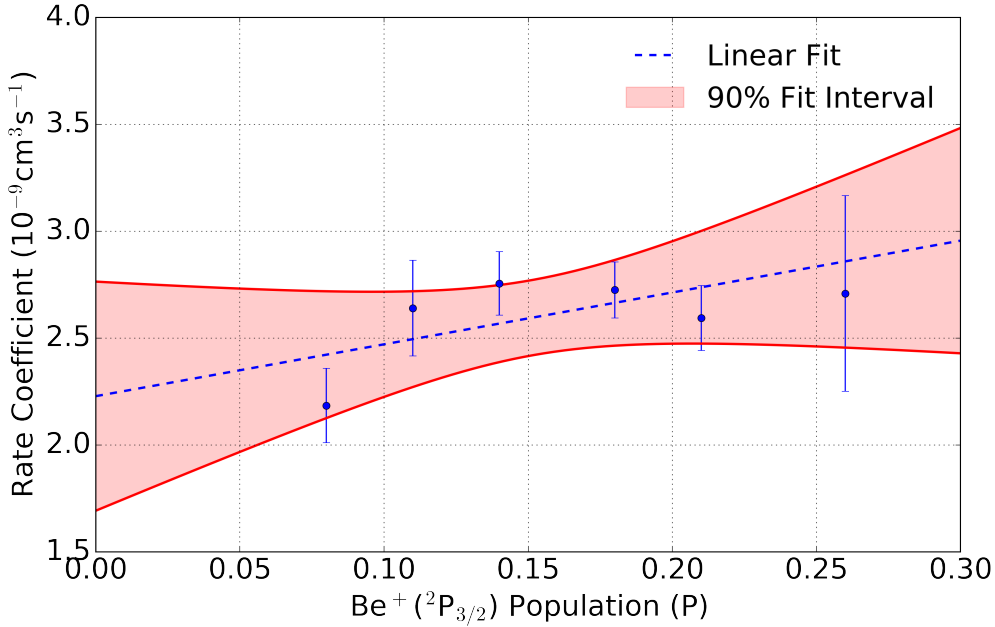


Figure 5.1:

where the ion-dipole interaction is averaged over rotational states. The expression for the rate coefficient from ADO theory is

$$k_{\text{ADO}} = 2\pi e \sqrt{\frac{\alpha}{\mu}} + 2\pi e \mu_D C \sqrt{\frac{2}{\mu \pi k_B T}} \quad (5.10)$$

where  $\alpha$  is the average neutral molecule polarizability,  $\mu$  is the reduced mass,  $\mu_D$  is the molecular dipole moment,  $e$  is the elementary charge, and  $C$  is the dipole locking constant. As a capture theory, ADO theory assumes that the reaction is dominated by long-range intermolecular forces, and when the ion moves inside the maximum of the centrifugal barrier, the reaction always proceeds with unit efficiency. The ADO model predicts that both the ground and excited Be+ states react with a rate coefficient of  $4.1 \times 10^{-9} \text{ cm}^3/\text{s}$  at 100 K reaction temperature, roughly two times larger than measured for the ground state, but in agreement with the measured reaction rate of the excited state. However, because it is long-range, the ADO model cannot provide the branching ratio and state-dependent information and is therefore insufficient for describing the observed reactions.

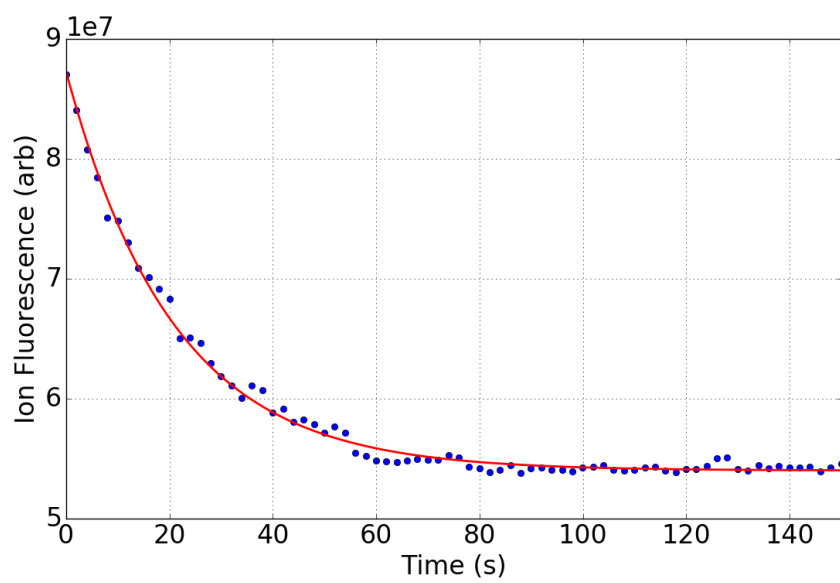


Figure 5.2:

# CHAPTER 6



## 6.1 Isotope-selective chemistry in the $\text{Be}^+(\text{^2S}_{1/2}) + \text{HOD} \longrightarrow \text{BeOD}^+ / \text{BeOH}$ H/D reaction

### 6.2 Abstract

Low temperature reactions between laser-cooled  $\text{Be}^+(\text{^2S}_{1/2})$  ions and partially deuterated water (HOD) molecules have been investigated using an ion trap and interpreted with zero-point corrected quasi-classical trajectory calculations on a highly accurate global potential energy surface for the ground electronic state. Both product channels have been observed for the first time, and the branching to  $\text{BeOD}^+ + \text{H}$  is found to be  $0.58 \pm 0.14$ . The experimental observation is reproduced by both quasi-classical trajectory and statistical calculations. Theoretical analyses reveal that the branching to the two product channels is largely due to the availability of open states in each channel.

### 6.3 Introduction

Together, isotope substitution and the measurement of the resulting product branching ratios provide important details about reaction dynamics and are often used to identify reaction pathways and understand bond-selective chemistry.[?, 10, 57] Important examples include X + HOD (X = H, F, Cl, O) reactions, where the branching ratios are experimentally controlled by selective excitation of the O–H or O–D bond.[41, 5, 30, 58, 45, 46, 15, 60, 42] It is now understood that a highly-accurate potential energy surface (PES) is crucial for performing

theoretical calculations of the product branching ratio, where subtle, difficult to identify, PES features have been found to significantly affect the results.[42]

A sophisticated understanding of radical-molecule reaction dynamics is continuing to develop from extensive experimental and theoretical studies. However, despite their importance in interstellar chemistry, where the isotopic branching ratios strongly influence the products of the interstellar cloud chemical network, far less progress has been made in the study of [14] ion–molecule reactions at low temperature. This is largely due to the challenges associated with both the experimental and theoretical approaches to these systems.[9, 12, 1, 3, 40, 43, 44] Experimental difficulties include a lack of quantum state preparation and readout techniques, while theoretical difficulties appear when treating dynamics dominated by the long range interaction between ions and molecules. Recently, several groups have employed cold ( mK) and fully-controlled laser-cooled trapped ions to address these experimental issues. For instance, isotope selectivity was probed in the reaction of laser-cooled Mg<sup>+</sup> with HD, and the [22] formation rate of MgD<sup>+</sup> was found to be 5 times greater than MgH<sup>+</sup>. This observation was ascribed to a dynamic mechanism in the exit channel of the reaction since statistical methods predict only a factor of approximately 2.[11] A similar experimental technique was applied to Ca<sup>+</sup> + HD reactions as well,[17] where the CaD<sup>+</sup> channel was found to have 1.5 times higher population than the CaH<sup>+</sup> channel; no detailed theoretical calculations have been performed for this system. With the help of laser-cooled ions, the initial quantum states are experimentally well controlled, but highly accurate PESs are still challenging to calculate with Mg<sup>+</sup> or Ca<sup>+</sup> ions due to the complexity of their electronic structures. The development of a more comprehensive understanding of ion–molecule reactions at low temperature will benefit from studies with less complex species that are amenable to theoretical treatment.

In this publication, we report a combined experimental and theoretical study of the effect of isotope substitution in an ion–polyatomic molecule reaction. A key objective is to understand the role of dynamics in such a reaction. Previous work on Be<sup>+</sup> + H<sub>2</sub>O showed that chemical dynamics resulting from a submerged barrier strongly affect the reaction, leading to a reduction of the overall reaction rate from the capture limit. The overestimation

by the capture model was thus taken as a sign that this reaction is not completely statistical, despite the existence of a deep BeH<sub>2</sub>O<sup>+</sup> potential well along the reaction path. In this work, we probe the dynamics by examining the product branching ratio, which is presumably controlled by the exit channel barriers. Such a measurement is much more sensitive to the determination of the overall rates. Interestingly, here we find that the measured deuteration fraction of the ionic products is in good agreement with quasi-classical trajectory (QCT) calculations on the ground state PES. Furthermore, the branching ratio can be explained by a statistical model based on complete energy randomization in the long-lived transition complex.

## 6.4 Experimental

The apparatus employed here has been described in detail elsewhere.<sup>25</sup> Briefly, laser ablation of metallic Be is used to produce Be<sup>+</sup> ions, which are trapped in a linear radio frequency Paul trap. Laser cooling<sup>26</sup> is used to cool the translational motion of the ions, resulting in a Coulomb crystal of Be<sup>+</sup> ions. A time-of-flight mass spectrometer (TOF-MS)<sup>27–30</sup> is integrated into the Paul trap to analyze reaction products, allowing investigation of the isotope effect by mass spectrometry of the trapped ionic products. The 313 nm laser for cooling Be<sup>+</sup> ions allows manipulation of the Be<sup>+</sup> electronic quantum states; by tuning the frequency of this cooling laser, the fraction of ions in the 2S1/2 and 2P3/2 states can be precisely controlled. Promotion of the Be<sup>+</sup> to the 2P3/2 state opens more product pathways, as well as modifies existing product channels.<sup>25</sup> HOD is made by mixing H<sub>2</sub>O and D<sub>2</sub>O.<sup>31,32</sup> The gaseous room-temperature HOD/H<sub>2</sub>O/D<sub>2</sub>O mixture is then introduced via a leak valve into the trapping region for reaction with the trapped ions, the actual ratio of the mixture is measured from a Stanford Research Systems (SRS) residual gas analyzer (RGA). The RGA's fractionation of water was calibrated by introducing the water vapor into the chamber and integrating all resulting m/z signals. A typical scan reveals water fractionation products at m/z = 18, 17, and 16, which coincide with H<sub>2</sub>O<sup>+</sup>, OH<sup>+</sup>, and O<sup>+</sup>. The fractionation ratios of water are found by solving the system of equations:

$$P_{\text{H}_2\text{O}} = R_{18} + R_{17} + R_{16} \quad (6.1)$$

$$R_{18} = \alpha P_{\text{H}_2\text{O}} \quad (6.2)$$

$$R_{17} = \beta P_{\text{H}_2\text{O}} \quad (6.3)$$

$$R_{16} = \gamma P_{\text{H}_2\text{O}} \quad (6.4)$$

where  $R_i$  is the pressure reading from the RGA and  $P_{\text{H}_2\text{O}}$  is the true  $\text{H}_2\text{O}$  pressure. These fragmentation ratios were found to be  $\alpha = 0.768 \pm 0.006$ ,  $\beta = 0.184 \pm 0.006$  and  $\gamma = 0.068 \pm 0.002$ . The direct readings from analog scans with deuterated samples were then adjusted to account for the fractionation for each isotopologue.

$$P_{\text{H}_2\text{O}} = \frac{1}{\alpha} \left( R_{18} - \frac{\beta}{\alpha} R_{20} - \frac{\beta}{2\alpha} R_{19} \right) \quad (6.5)$$

$$P_{\text{HOD}} = \frac{R_{19}}{\alpha} \quad (6.6)$$

$$P_{\text{D}_2\text{O}} = \frac{R_{20}}{\alpha} \quad (6.7)$$

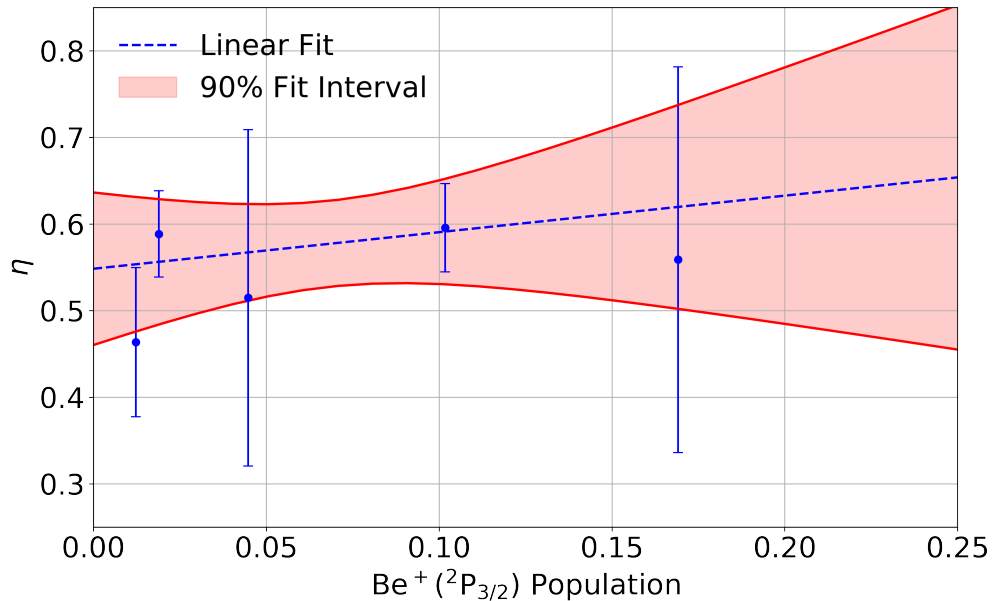


Figure 6.1:

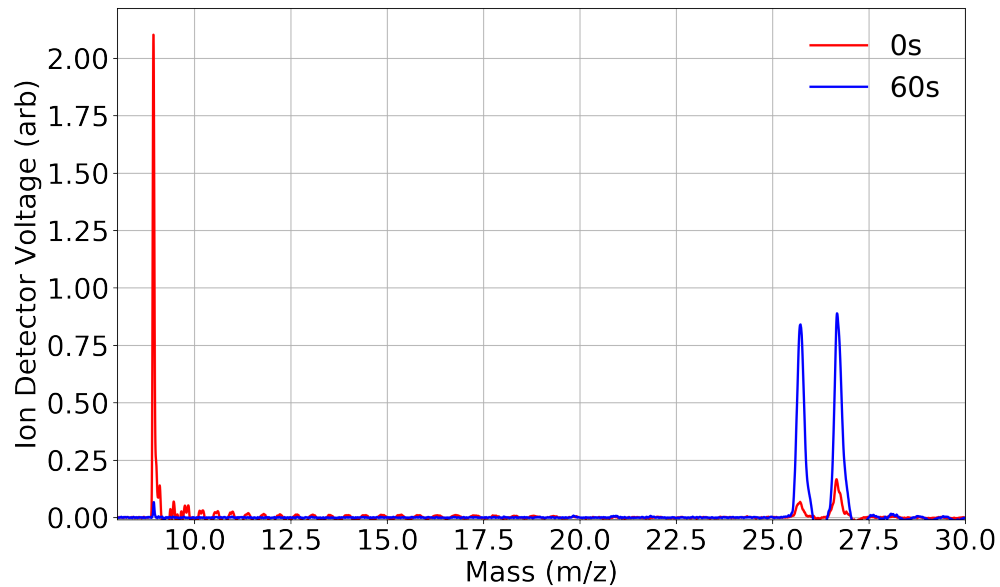


Figure 6.2:

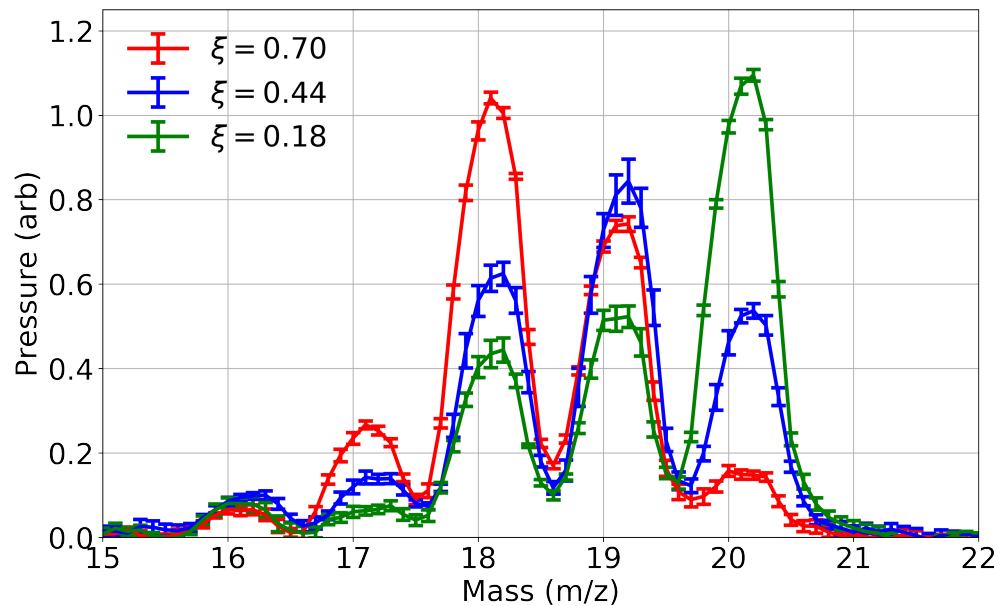


Figure 6.3:

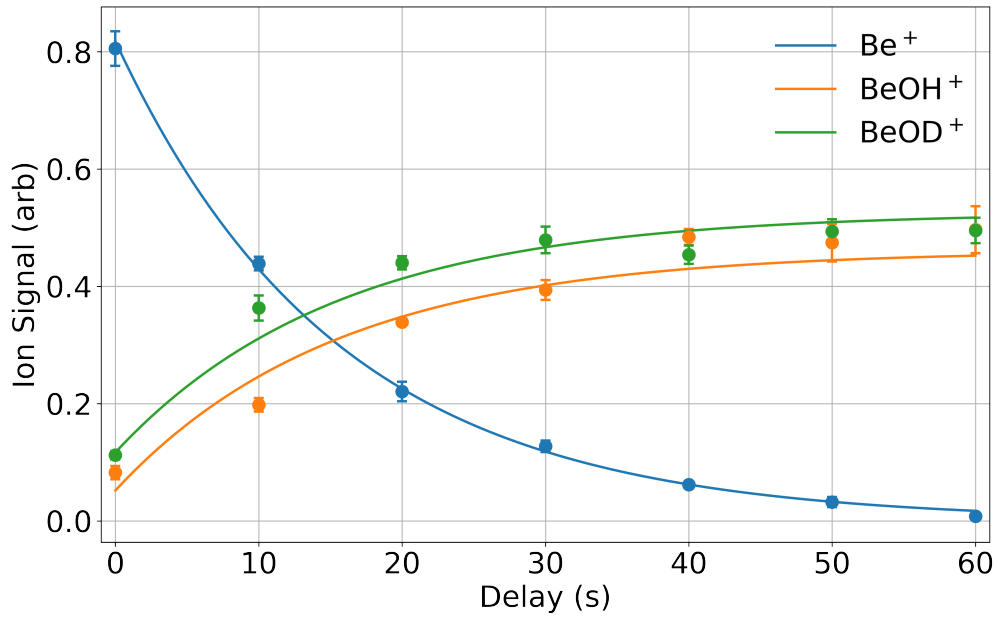


Figure 6.4:

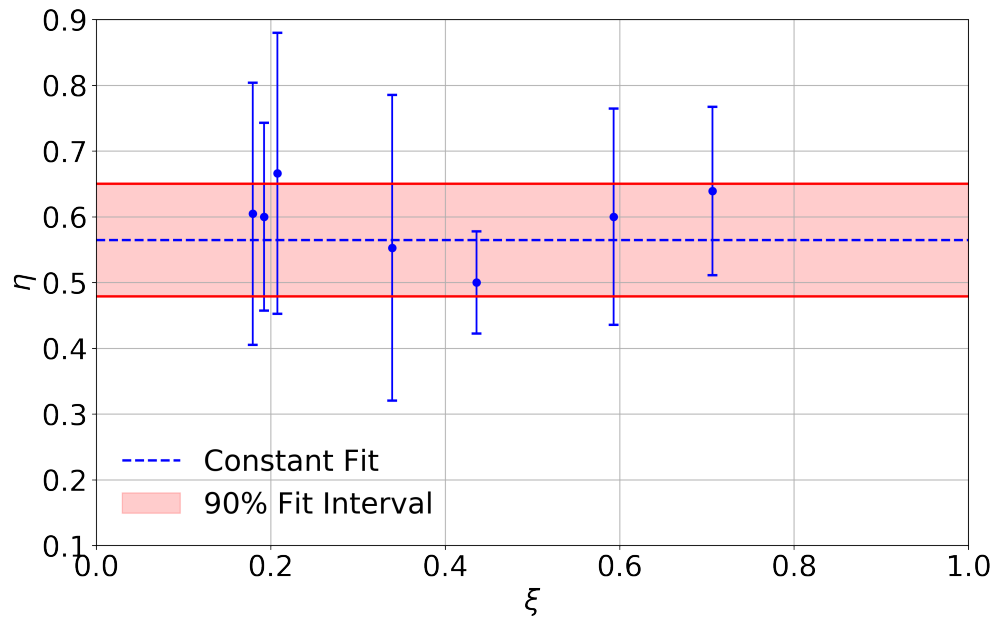
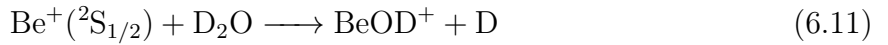
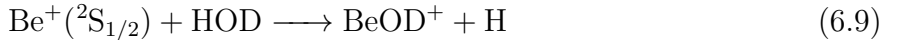
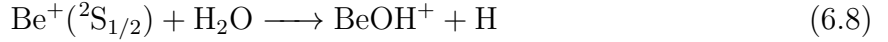


Figure 6.5:

## 6.5 Results and Discussion

Because the HOD sample also contains both  $\text{H}_2\text{O}$  and  $\text{D}_2\text{O}$ , the product  $\text{BeOH}^+$  ( $m/z = 26$ ) has contributions of the reaction of the cation with  $\text{H}_2\text{O}$ , while  $\text{BeOD}^+$  ( $m/z = 27$ ) has contributions from reactions with  $\text{D}_2\text{O}$ . The reactions of interest are:



Thus, the kinetics of the reagents and products are found from:

$$\text{Be}^+(t)' = (k_1\rho_1 + k_2\rho_2 + k_3\rho_3)\text{Be}^+(t) \quad (6.12)$$

$$\text{BeOH}^+(t)' = (k_1\rho_1 + (1 - \eta)k_2\rho_2)\text{Be}^+(t) \quad (6.13)$$

$$\text{BeOD}^+(t)' = (k_3\rho_3 + \eta k_2\rho_2)\text{Be}^+(t) \quad (6.14)$$

where  $k_i$  and  $r_i$  are the rate coefficient and density for  $\text{Be}^+$  reacting  $\text{H}_2\text{O}$ , HOD, and  $\text{D}_2\text{O}$  respectively. The branching ratio  $\eta \equiv k_{\text{BeOD}^+}/(k_{\text{BeOD}^+} + k_{\text{BeOH}^+})$  is the fraction of  $\text{BeOD}^+$  produced from reactions (4.2) where  $k_j$  is the rate coefficient of species  $j$ . Solutions to the rate equations (4.4)–(4.6) are parameterized by the density measurements of the water isotopologues taken from a RGA, and a least-squares fit is taken over data sets of integrated TOF mass spectra with shared fitting parameters  $k_1$ ,  $k_2$ ,  $k_3$ , and  $\eta$ . In order to extract the pure  $\text{Be}^+(\text{S}_{1/2})$  and  $\text{Be}^+(\text{P}_{3/2})$ -state branching ratios, the process shown in Fig. 1(A)–(C) was repeated at different P-state fractions. The results are shown in Fig. 1(D) along with a least-squares linear-fit (blue line). The vertical intercept of this fit gives  $\eta_S = 0.56 \pm 0.03$  for the ground  $\text{Be}^+(\text{S}_{1/2})$  state reaction, while no conclusive dependence on P-state fractions is found within the confidence intervals. To further verify that our measurement is independent

of reagent ratios, we repeated the measurement for different mixtures of HOD, H<sub>2</sub>O, and D<sub>2</sub>O, as shown in Fig. 3. The branching ratio of BeOD<sup>+</sup> + H in reaction Be<sup>+</sup> + HOD (with 2% Be<sup>+</sup>(<sup>2</sup>P<sub>3/2</sub>) state population) is consistent over different hydrogen fractions in the gas. The fraction of hydrogen atoms in the chamber ( $\xi$ ) from all water isotopologues is defined by:

$$\xi = \frac{2\rho_{\text{H}_2\text{O}} + \rho_{\text{HOD}}}{\rho_{\text{H}_2\text{O}} + \rho_{\text{HOD}} + \rho_{\text{D}_2\text{O}}} \quad (6.15)$$

Weighted averaging of the fitted values over different mixtures then gives  $\eta = 0.58 \pm 0.14$ ,  $k_2/k_1 = 0.8 \pm 0.9$ ,  $\frac{k_3}{k_1} = 0.8 \pm 0.9$ . Despite the large error bars on the relative rate coefficients, due to the significant covariance of the rate coefficients,  $\eta$  is reasonably well determined. To further check our measurement of  $\eta$ , the process was repeated for shared fits with identical rate coefficients ( $k_1 = k_2 = k_3$ ) yielding  $\eta = 0.57 \pm 0.07$ . The calculated overall rate coefficients of the Be<sup>+</sup> + D<sub>2</sub>O and Be<sup>+</sup> + HOD reactions are  $(2.29 \pm 0.05) \times 10^{-9}$  cm<sup>3</sup> molecule<sup>-1</sup> s<sup>-1</sup> and  $(2.29 \pm 0.05) \times 10^{-9}$  cm<sup>3</sup> molecule<sup>-1</sup> s<sup>-1</sup>, respectively, which are slightly larger than that  $((2.02 \pm 0.04) \times 10^{-9}$  cm<sup>3</sup> molecule<sup>-1</sup> s<sup>-1</sup>)25 of the Be<sup>+</sup> + H<sub>2</sub>O reaction. The calculated  $k_2/k_1$  and  $k_3/k_1$  ratios are  $1.13 \pm 0.04$  and  $1.13 \pm 0.04$ , which are consistent with experimental values of  $0.8 \pm 0.9$  and  $0.8 \pm 0.9$ , respectively. The identical  $k_2/k_1$  and  $k_3/k_1$  ratios suggests the negligible isotopic effect in the thermal reaction probabilities of the Be<sup>+</sup> + D<sub>2</sub>O and Be<sup>+</sup> + HOD reactions. The branching ratio was determined using the QCT method for the Be<sup>+</sup> + HOD reaction. Specifically, the calculated branching fraction of Be<sup>+</sup> + HOD ( $\eta$ ) is  $0.61 \pm 0.02$ , which is in good agreement with experimental value  $0.58 \pm 0.14$ . The branching ratio of the two products (BeOD<sup>+</sup> and BeOH<sup>+</sup>) can be understood in terms of the PST model, which assumes complete energy randomization in the deep intermediate (BeHOD<sup>+</sup>) well. In Fig. 4, the branching fraction for the BeOD<sup>+</sup> + H channel is plotted as a function of the collision energy, which shows very weak temperature dependence. At the specific collisional temperature 100K, the fraction obtained by integrating the energy dependent branching ratio with a Boltzmann weight is 0.67, which is in reasonable agreement with the QCT results.

To shed more light onto the preference of the  $\text{H} + \text{BeOD}^+$  channel in the  $\text{Be}^+ + \text{HOD}$  reaction, we provide a further analysis of the two important factors in determining the branching ratio. In PST, the reactivity in a particular product channel is controlled by the availability of open states, which is in turn dictated by the rovibrational states of the corresponding product molecule above the exit barrier formed by the centrifugal potential. Due to the heavier deuterium, it is readily understood that there are more rovibrational states for  $\text{BeOD}^+$  than  $\text{BeOH}^+$ . However, the availability of open channels is also constrained by the orbital angular momentum ( $l$ ), which erects a centrifugal barrier in both the reactant and product channels. The  $l$ -dependent centrifugal barrier is also isotope dependent, due to the difference in the reduced mass between the two products. The centrifugal barrier rises faster in the  $\text{BeOD}^+ + \text{H}$  channel than the  $\text{BeOH}^+ + \text{D}$  channel, due to the larger reduced mass of the latter. This is consistent with the fact that the branching fraction ( $\eta$ ) of  $\text{BeOD}^+ + \text{H}$  channel becomes larger when the centrifugal barrier was not considered (shown in Fig. 4). These two factors have opposing effects on the branching ratio, but the higher density of states in the  $\text{BeOD}^+$  molecule dominates, at least at low energies. As a result, the  $\text{H} + \text{BeOD}^+$  product channel is strongly favored. The good agreement of the statistical model with both the experimental and QCT results in branching ratio suggests that the reaction is largely statistical. In addition, the DCSs of the  $\text{Be}^+ + \text{H}_2\text{O}/\text{HOD}/\text{D}_2\text{O}$  reactions calculated by the QCT method are shown in Fig. 5. It can be seen from the figure that the DCSs of all three reactions are roughly forward–backward symmetric, due to the long-lived intermediates formed in the reactions. The forward–backward symmetry in DCSs suggests the statistical nature of the reaction, which further validates the suitability of the PST model discussed above.

## 6.6 Conclusion

To summarize, chemical reactions between  $\text{Be}^+(^2\text{S}_{1/2})$  and HOD have been investigated using an integrated ion trap and highresolution TOF-MS and ZPE corrected QCT calculations on an accurate global PES. Two product channels have been observed and the branching to

$\text{BeOD}^+ + \text{H}$  is accurately determined to be  $0.58 \pm 0.14$ . The experimental result is in good agreement with ZPE corrected QCT calculation result ( $0.61 \pm 0.02$ ) as well as close to the statistical PST model ( 0.67), which reveals that the branching to the two product channels is largely due to the availability of different open states in each channel. Since their rate coefficients deviate from the capture limit as reported in our earlier work, it is clear that the  $\text{Be}^+(2\text{S}_{1/2}) + \text{H}_2\text{O}/\text{D}_2\text{O}/\text{HOD}$  reactions have a non-negligible non-statistical component. Interestingly, however, the good prediction of the branching ratio by the statistical model discussed above suggests that the formation of the products is largely statistical. This conclusion is further supported by the forward–backward symmetry of the calculated DCSs.

## 6.7 Notes

We mix "equal" amounts of  $\text{H}_2\text{O}$  and  $\text{D}_2\text{O}$  and leave it overnight to produce roughly 1:2:1 ratio of  $\text{H}_2\text{O}:\text{HOD}:\text{D}_2\text{O}$  as roughly verified by the RGA. If we consider being a singular oxygen atom looking at a sea of  $\text{H}_2\text{O}$  and  $\text{D}_2\text{O}$ , it has a 1/4 probability of grabbing H or D twice. It then has a 1/2 chance of grabbing an H and D in either order, which gives us the 1:2:1 ratio.

To generalize this, we can write the fraction of  $\text{H}_2\text{O}$  in the sample to be  $\gamma$  and the  $\text{D}_2\text{O}$  to be  $1 - \gamma$ . The probabilities of yielding any combination is then found quickly:

$$\text{H}_2\text{O} = \gamma^2 \quad (6.16)$$

$$\text{HOD} = 2\gamma(1 - \gamma) \quad (6.17)$$

$$\text{D}_2\text{O} = (1 - \gamma)^2 \quad (6.18)$$

For the sake of readability, let  $(\text{H}_2\text{O}, \text{HOD}, \text{D}_2\text{O})$  be represented as  $(1, 2, 3)$  respectively.

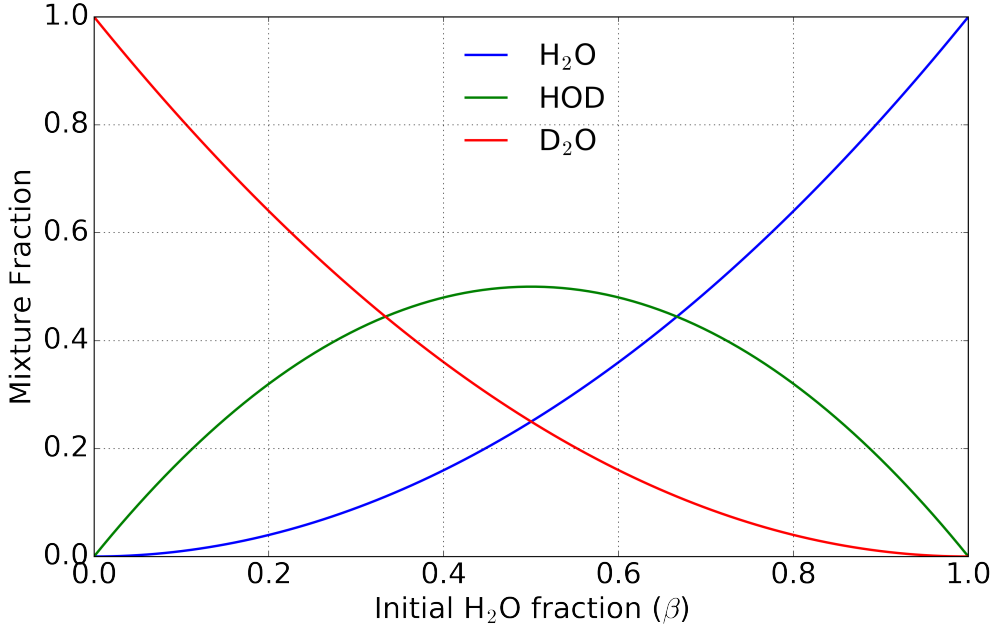


Figure 6.6:

Reading water with an RGA causes some known fractionation, where the  $H_2O$  is broken into its constituents, including  $OH^+$  and  $O^+$ . We expect then to see a lower mass 18 peak than normal, to truly know what the ratios are, we have to calibrate the RGA ourselves.

Possible fractionation pathways:

$$P'_{18} = \alpha P_{H_2O} + \beta \left( \frac{P_{HOD}}{2} + P_{D_2O} \right) \quad (6.19)$$

$$P'_{19} = \alpha P_{HOD} \quad (6.20)$$

$$P'_{20} = \alpha P_{D_2O} \quad (6.21)$$

$$P'_{17} = \beta \left( \frac{P_{HOD}}{2} + P_{H_2O} \right) \quad (6.22)$$

$$P'_{16} = \gamma (P_{H_2O} + P_{HOD} + P_{D_2O}) \quad (6.23)$$

$$1 = \alpha + \beta + \gamma \quad (6.24)$$

By solving this system of equations, we get 76.8% of the real value as cited by the RGA program itself; this is also true for HOD and  $D_2O$ . Of that lost 23.2%, 18.4% goes to  $OH^+$ ,

but for the isotopogues of HOD and D<sub>2</sub>O, we would need to consider which mass signal it will add to. No other mode of fractionation will contribute to the other water isotopologue peaks

$$P'_1 = \alpha P_1 + \beta P_3 + \frac{\beta}{2} P_2 \quad (6.25)$$

$$P'_2 = \alpha P_2 \quad (6.26)$$

$$P'_3 = \alpha P_3 \quad (6.27)$$

Where we let  $\alpha = 0.744$  and  $\beta = 0.256$  per the SRS RGA software. Where P is the real pressure accounting for fractionation, and P' is the raw observed pressure value. Solving for the real pressure, we find:

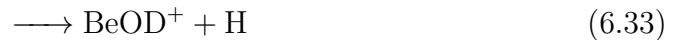
$$P_1 = \frac{1}{\alpha} \left( P'_1 - \frac{\beta}{\alpha} P'_3 - \frac{\beta}{2\alpha} P'_2 \right) \quad (6.28)$$

$$P_2 = \frac{P'_2}{\alpha} \quad (6.29)$$

$$P_3 = \frac{P'_3}{\alpha} \quad (6.30)$$

## 6.8 Be<sup>+</sup> + HOD branching ratio

Now that we can characterize the pressures in the chamber more accurately, we then consider the possible reactions between the Be<sup>+</sup> and water isotopologues:



Which can then be written as a system of differential equations.

$$\dot{Be}(t) = -(k_1\rho_1 + k_2\rho_2 + k_3\rho_3)Be(t) \quad (6.35)$$

$$\dot{BeOH}(t) = (k_1\rho_1 + (1 - \eta)k_2\rho_2)Be(t) \quad (6.36)$$

$$\dot{BeOD}(t) = (k_3\rho_3 + \eta k_2\rho_2)Be(t) \quad (6.37)$$

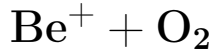
We are interested in reactions 6.32 and 6.33 and the ratio between the two ( $\eta$ ), which is not directly found from the ratio of the production rates of the two ions. Since this is a ratio, we don't need to concern ourselves with calculating the density ( $\rho$ ), the RGA pressure is fine.

$$\beta \equiv \frac{\dot{BeOD}}{\dot{BeOH}} = \frac{k_3P_3 + \eta k_2P_2}{k_1P_1 + (1 - \eta)k_2P_2} \quad (6.38)$$

$$\eta = \frac{\beta(k_1P_1 + k_2P_2) - k_3P_3}{k_2P_2(1 + \beta)} \quad (6.39)$$

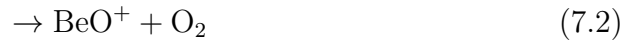
The theorists found that the statistical value of the reaction is around 3, but with dynamics, tends towards  $\frac{\eta}{1-\eta} = 1.7$  or  $\eta = 0.63$  for  $\text{Be}^+(\text{S})$ .

## CHAPTER 7



Beryllium metal is ablated with an Nd:YAG laser and trapped in a linear Paul trap. Laser cooling is applied with a 313nm laser. Pure O<sub>2</sub> gas is introduced into the chamber via leak valve to react with the ions. Remaining reactants and charged reaction products are ejected into a time-of-flight mass spectrometer (TOF) where the various masses of ions can be determined.

When the Be<sup>+</sup> is excited from the <sup>2</sup>S<sub>1/2</sub> to the <sup>2</sup>P<sub>3/2</sub> manifold, we find the energetically allowed channels to be:



Without excitation into the <sup>2</sup>P<sub>3/2</sub> manifold, reactions 7.1 and 7.2 are endothermic by 2.75eV and 1.1eV, respectively.

Despite the fact that reaction 7.2 is energetically allowed, it is never seen with laser cooling.

Without 313nm light, the Be<sup>+</sup> ions stay in the <sup>2</sup>S<sub>1/2</sub> ground state, but with a ion trap depth > 4eV, there are portions of the ion cloud with enough energy to still proceed with the production of BeO<sup>+</sup>. Without the laser cooling, we observe the disappearance of BeO<sup>+</sup>

from the trap due to exciting the molecule into a pre-dissociative state.

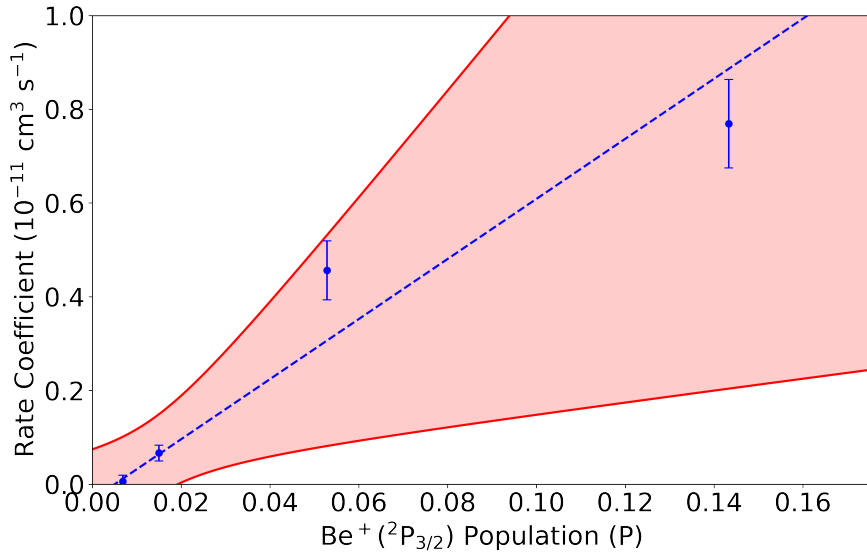


Figure 7.1: A linear dependence on the rate constant for reaction 7.1 as a function of P state excitation.  $k = (6 \pm 1) \times 10^{-11}P + (-0.03 \pm 0.16) \times 10^{-11}$

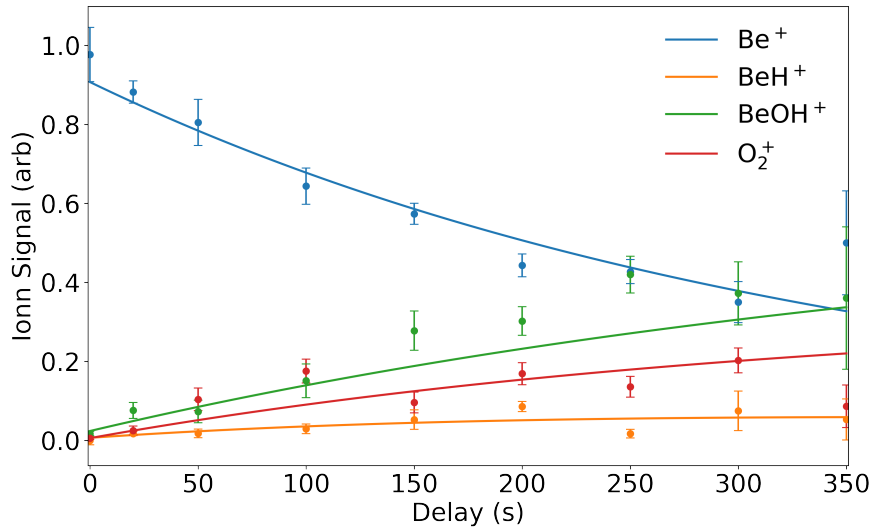


Figure 7.2: Shared fitting of trapped products with 14% p-state excitation.

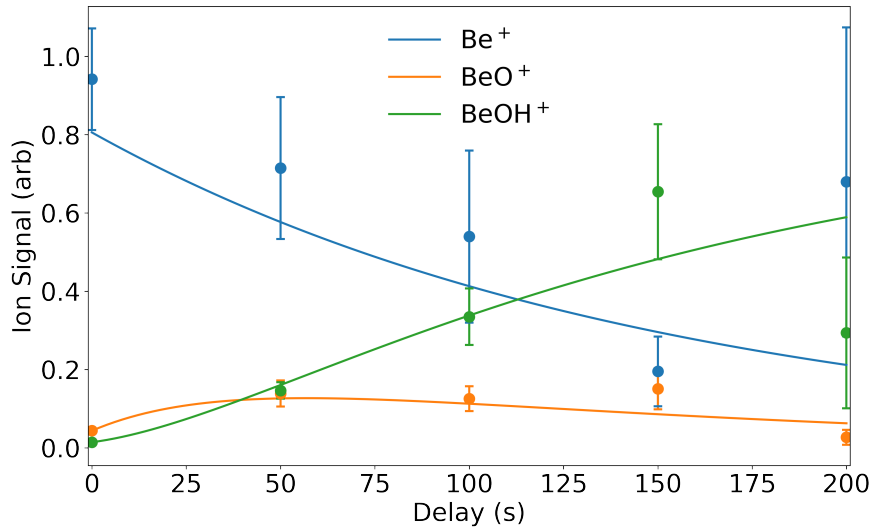


Figure 7.3: Shared fitting of trapped products with 14% p-state excitation.

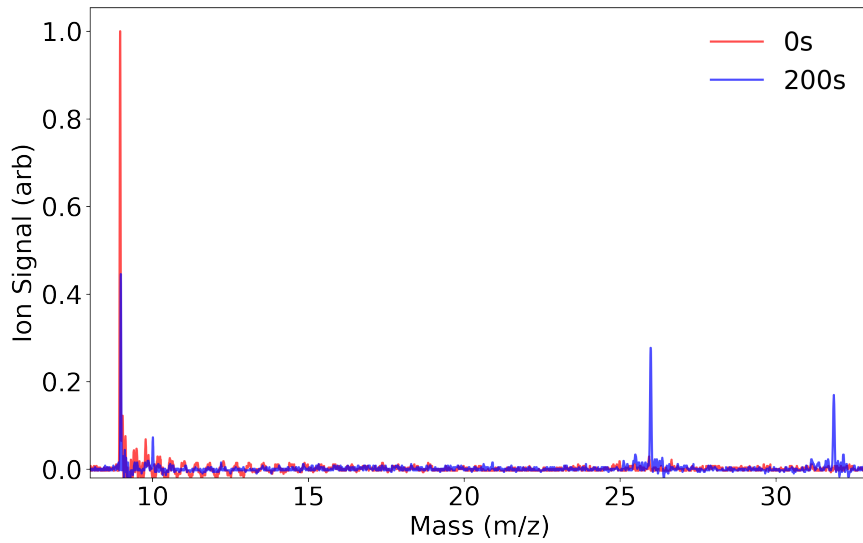


Figure 7.4: TOF traces for data taken with 14% p-state excitation at 0s and 200s showing no products at 0s, but distinct peaks for reaction products  $\text{BeH}^+$ ,  $\text{BeOH}^+$ , and  $\text{O}_2^+$ .

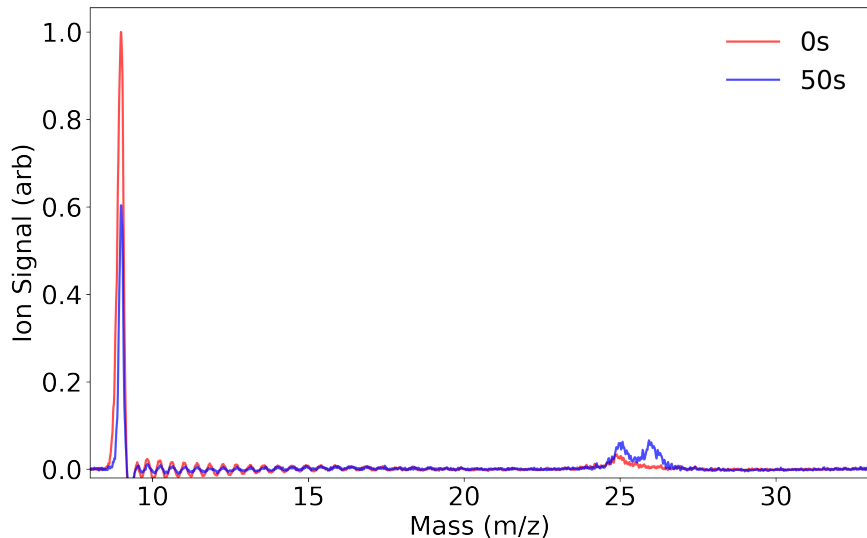


Figure 7.5: TOF traces for data taken with 14% p-state excitation at 0s and 200s showing no products at 0s, but distinct peaks for reaction products  $\text{BeH}^+$ ,  $\text{BeOH}^+$ , and  $\text{O}_2^+$ .

Considering state counting, reactions ?? and ?? have been measured to have branching ratios that vary from 60:40 ( $\text{CO}^+:\text{O}^+$ ) to 30:70 in the other direction. By looking at experimental data as well as the theoretical state counting, we find the ratio to be pretty definitively 60:40.

# CHAPTER 8



## 8.1 Formyl Isomer Branching Ratio

With our dual ablation system, we can reliably co-trap carbon and beryllium ions and introduce cold molecules from the CBGB. Introducing water entrained in a cold neon buffer gas beam, we can see the reaction products due to these collisions. The internal temperature of the buffer gas in the beam is verified to be, which is defined by the temperature of the inner cell.

We do not expect any reactions to occur with the cold neon buffer gas. We have experimentally verified the absence of new mass peaks when introducing neon into the system with carbon and beryllium ions, only an overall loss rate attributed to elastic collisions within the trap.

Conversely, the water molecules will react readily with both beryllium and carbon ions, where the prevailing beryllium reactions are eqs. (5.1) to (5.3). Considering the known reaction products of  $\mathbf{C}^+ + \mathbf{H}_2\mathbf{O}$ :



Add  
graphs  
of  
flu-  
o-  
res-  
cence  
de-  
cay

$$C(t) = C_0 e^{-k_1 \rho t} \quad (8.4)$$

$$[HCO](t) = \frac{e^{-(k_1+k_2)\rho t}}{k_1 - k_2} (e^{k_1 \rho t} ((C_0 + [HCO]_0)k_1 - [HCO]_0 k_2) - C_0 e^{-(k_1+k_2)\rho t}) \quad (8.5)$$

$$H_3O(t) = \frac{([HCO]_0 e^{-k_2 \rho t} - (H_3O_0 + [HCO]_0)) (k_2 - k_1) + C_0 (k_1 (1 - e^{-k_2 \rho t}) + k_2 (e^{-k_1 \rho t} - 1))}{k_1 - k_2} \quad (8.6)$$

We want to probe the branching ratio of the formyl isomers formed in reactions 8.1 and 8.2 at low temperatures. At room temperatures, the branching ratio has been found to be approximately 84:16 ( $\text{COH}^+$ : $\text{HCO}^+$ )[14], but unexplored at lower regimes.

By definition, these formyl isomers of reactions eqs. (8.1) and (8.2) have identical mass and thus, cannot be readily read off by the TOF system. To be able to separate the isomer products, we need to be able to separate their masses. By introducing a gas into the system with a proton affinity in between the isomer products, we may selectively react only one the less stable  $\text{COH}^+$  isomer. This also yields a distinct  $m/z$  peaks due to each isomer. By using an external gas, we are doing an indirect measurement, and as such, it may add unintended complications. Certain gasses are more reactive and may react with the excited  $\text{Be}^+$ ,  $\text{C}^+$ , or any other ionized species in the trap. Another possibility is that the  $\text{COH}^+$  may isomerize due to interactions with the gas(8.7).[13]



	Affinity (kcal/mol)
CO*	427
Kr	425
HF	490
N <sub>2</sub>	495
Xe	496
NO	531
CO <sub>2</sub>	548
CH <sub>4</sub>	552
HCl	564
HBr	569
N <sub>2</sub> O	571
*CO	594

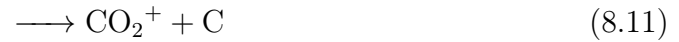
Table 8.1: Proton affinities of gasses between formyl isomers where (\*) indicates H bonding location.

Previous literature utilized gasses such as NO, CH<sub>4</sub>, N<sub>2</sub>O, and Kr to perform similar titrations. Kr, and Xe are inert and would not react with any other trapped ion but are too heavy to reliably trap after a reaction. NO is caustic and will ruin the vacuum chamber if introduced, and thus was avoided. Attempts were made with N<sub>2</sub>O and well as CH<sub>4</sub>, but both had issues. N<sub>2</sub>O rapidly reacts with Be<sup>+</sup> and made reliable TOF traces unattainable due to the loss of coolant ion. CH<sub>4</sub> readily reacted with most of the ions in the trap to produce a multitude of mass peaks, greatly complicating the analysis. At the end, success was found with CO<sub>2</sub> and <sup>15</sup>N<sub>2</sub>.

## 8.2 CO<sub>2</sub> Titration

From table 8.1, we see that CO<sub>2</sub> is a viable option to titrate the reaction products. The possible reactions of CO<sub>2</sub> with Be<sup>+</sup> are unknown in literature, but found to be non-reactive

in both ground and excited states, while  $\text{C}^+$  readily reacts.



Testing the purity of the  $\text{CO}_2$ , I introduce the  $\text{CO}_2$  into the ion chamber with the RGA.

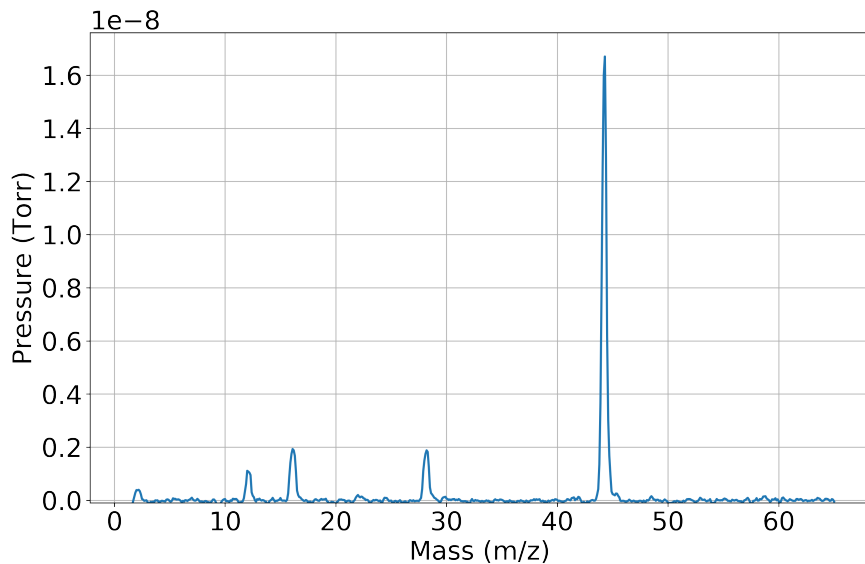


Figure 8.1: RGA showing purity of  $\text{CO}_2$  introduced into chamber. Ratios of  $\text{CO}_2$  peaks at  $m/z = 12, 16, 28$ , and  $44$  in agreement with table 8.2, with no conclusive evidence of contamination by any other gas.

m/z	Fraction
44	0.85
28	0.05
16	0.05
12	0.012

Table 8.2: RGA fractionation of CO<sub>2</sub> as given by  
<http://ytonline.com/technical-information/rga-spectra-data-fragmentation-factor/>

### 8.2.1 Be<sup>+</sup> + CO<sub>2</sub>

Introducing the CO<sub>2</sub> into the ion chamber to react with only laser cooled Be<sup>+</sup>, The TOF only shows that there are trace amounts of H<sub>2</sub>O in the chamber, with no indication of any further loss due to the inclusion of CO<sub>2</sub>.

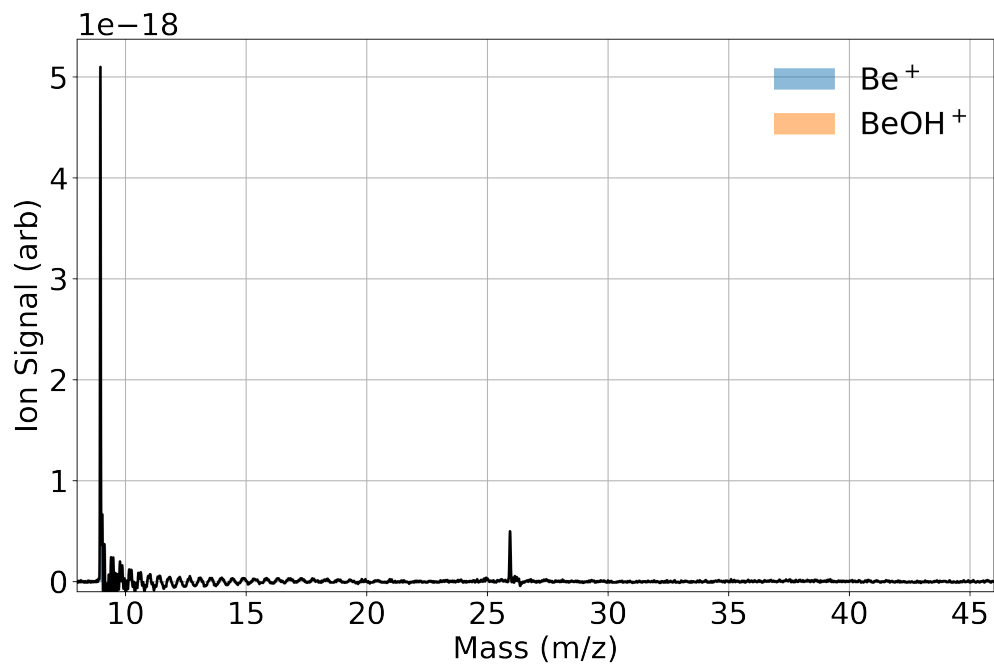


Figure 8.2: TOF trace of laser-cooled Be<sup>+</sup> reacting with  $\approx 1 \times 10^{-8}$  Torr CO<sub>2</sub> introduced via leak valve for 50 seconds.

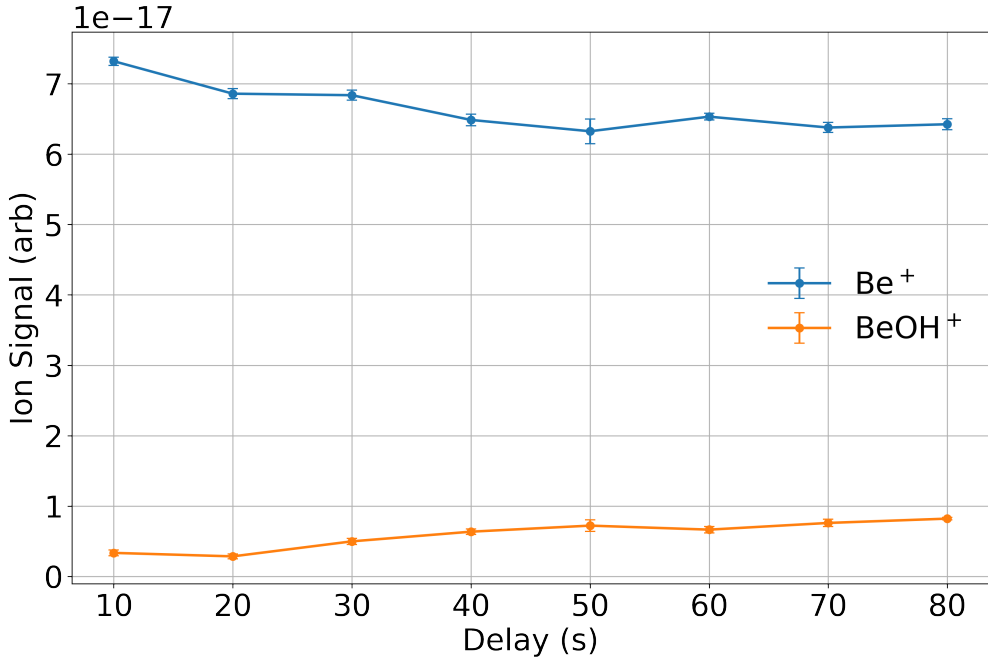


Figure 8.3: Integrated ion signal of individual TOF traces normalized by  $\text{Be}^+$  fluorescence at various  $\text{CO}_2$  exposure times.

We see that there aren't any reactions happening between  $\text{Be}^+$  and  $\text{CO}_2$ , while there is a little bit of water in the leak valve, which was baked afterwards. This does indicate that there are also no reactions between  $\text{BeOH}^+$  and  $\text{CO}_2$ .

### 8.2.2 $\text{C}^+ + \text{CO}_2$

By ablating both  $\text{C}^+$  and  $\text{Be}^+$  into the trap and introducing  $\text{CO}_2$  via the leak valve, we find the expected reactions 8.10, 8.11, and 8.12 as well as unexpected peaks appearing at  $m/z = 15, 29$ , and  $45$ .

Labels in figures sections 8.2.2 and 8.2.2 are of predicted chemicals coinciding with the masses. The initial guess is that there is  $\text{H}_2\text{O}$  in the leak valve, as we saw it before in the  $\text{Be}^+ + \text{CO}_2$  reaction, but the leak valve region was baked since that data was taken. Similarly, if there was water, we would see a peak at  $m/z = 26$ , coinciding with  $\text{BeOH}^+$ , which we do not see, we should also expect to see an abundance of  $\text{H}_3\text{O}^+$  due to reactions between the

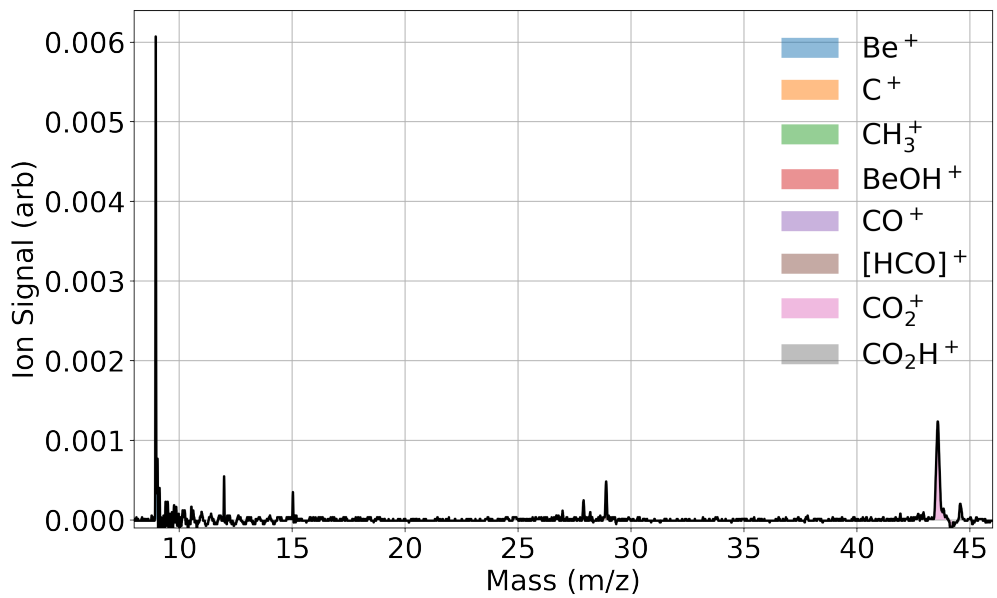


Figure 8.4: TOF trace of laser-cooled  $\text{Be}^+$  and  $\text{C}^+$  reacting with  $\approx 1 \times 10^{-8}$  Torr  $\text{CO}_2$  introduced via leak valve for 40 seconds.

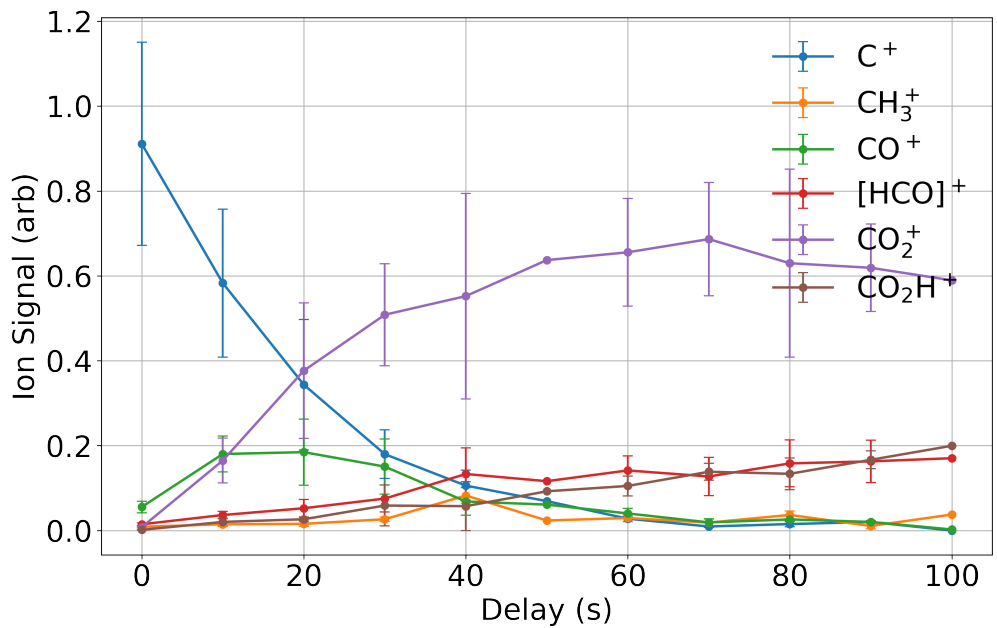


Figure 8.5: Integrated ion signal of individual TOF traces normalized by total ion signal excluding  $\text{Be}^+$  at various  $\text{CO}_2$  exposure times.

alleged  $[HCO]^+$  and  $CO_2H^+$ , which we also do not see. But, the peak at 45 could possibly be explained by  $H_2O$  in reaction 8.14, while 29 could be due to reactions 8.2 and 8.1. But there are no reactions with  $H_2O$  for the production of 15.



I still doubt that the 29 mass is due to  $C^+$  directly reacting with  $H_2O$  because the traces clearly show it increasing despite the depletion of  $C^+$ , indicating it is a second order reaction. It wouldn't be  $H_2$  either, because we would see  $BeH^+$  in the trap, as well as many other peaks associated with  $C^+ + H_2$  including 14, 16, and 17.

### 8.2.3 $Be^+ + C^+ + H_2O$ with $CO_2$

Water is introduced into the chamber via the CBGB with the cell held at a temperature of 20K. After  $(10 \pm 1)$  seconds of exposure, the gate valve is closed and  $CO_2$  is leaked in to react away the formyl isomers such that  $\approx 99\%$  are reacted away (determined by the disappearance of  $C^+$ ).

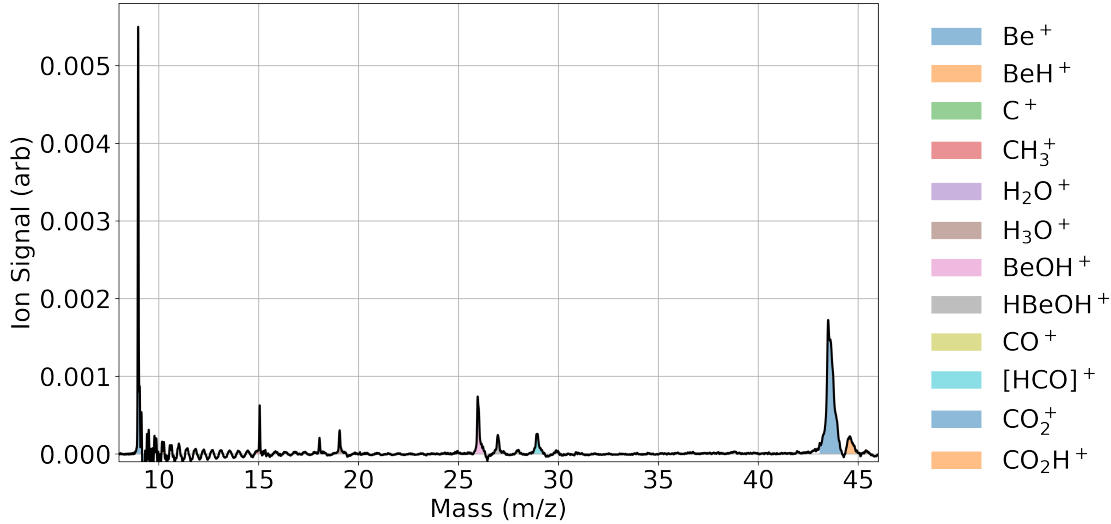


Figure 8.6:  $\text{C}^+$  and  $\text{Be}^+$  loaded into the trap is reacted with  $\text{H}_2\text{O}$  introduced from the beam. The gate valve is closed after 10 seconds and  $\text{CO}_2$  is introduced via leak valve so that the  $\text{COH}^+$  is titrated into  $\text{CO}_2\text{H}^+$ .

Knowing the anomalous peaks in the previous tests, the peaks of interest are not exclusively the branching ratio between the formyl isomers, where we define  $\gamma$  as the fraction of products that produce  $\text{COH}^+$ .

Solving the differential equations of the  $\text{C}^+ + \text{H}_2\text{O}$  reactions (eqs. (8.2), (8.1) and (8.3)), we may derive the equations of the ion reactions:

We define the ratio of the formyl isomers and remaining  $\text{C}^+$

$$\alpha(t) \equiv \frac{[\text{HCO}](t)}{[\text{HCO}](t) + \text{C}(t)} \quad (8.16)$$

In the data taken, we introduced the water in the beam for approximately 10s, the fraction of  $\text{C}^+$  that has turned into  $[\text{HCO}]^+$  is thus  $\alpha = 0.37 \pm 0.02$ . Considering that after titration with  $\text{CO}_2$ , the fraction of the remaining 63% of  $\text{C}^+$  has turned into equal amounts of  $m/z = 29, 45$  defined as  $\beta = 0.17 \pm 0.02$ .

$$N_C(0) = N_0 \quad (8.17)$$

$$N_C(\tau_1) = (1 - \alpha)N_0 \quad (8.18)$$

$$N_{29}(\tau_1) = \alpha N_0 \quad (8.19)$$

Where  $N_C(t)$  is the amount of  $\text{C}^+$  is in the trap after being exposed to either the water beam or  $\text{CO}_2$  for time  $t$ .  $\tau_1$  is the amount of time where the ions are exposed to the water beam, where  $\alpha$  is the proportion of  $\text{C}^+$  that is converted to  $m/z = 29$ , which in our case is 0.37. We then introduce the  $\text{CO}_2$  into the system and yield:

$$N_C(\tau_1 + \tau_2) = 0 \quad (8.20)$$

$$N_{29}(\tau_1 + \tau_2) = N_{29}(\tau_1)(1 - \gamma) + N_C(\tau_1)\beta \quad (8.21)$$

$$= N_0(\alpha(1 - \gamma) + \beta(1 - \alpha)) \quad (8.22)$$

$$N_{45}(\tau_1 + \tau_2) = N_{29}(\tau_1)\gamma + N_C(\tau_1)\beta \quad (8.23)$$

$$= N_0(\alpha\gamma + \beta(1 - \alpha)) \quad (8.24)$$

In conjunction with the ratio  $\eta \equiv \frac{\text{CO}_2\text{H}^+}{\text{CO}_2\text{H}^+ + \text{HCO}^+} = 0.55 \pm 0.02$

$$\eta = \frac{N_{45}(\tau_1 + \tau_2)}{N_{29}(\tau_1 + \tau_2) + N_{45}(\tau_1 + \tau_2)} \quad (8.25)$$

But we know that there are contributions to both masses of interest due to the inclusion of the  $\text{CO}_2$ , thus, we need to solve for  $\gamma$ :

$$\eta = \frac{\beta - \alpha\beta + \alpha\gamma}{\alpha + 2\beta - 2\alpha\beta} \quad (8.26)$$

$$\gamma = \frac{1}{\alpha}(\alpha\eta + \beta(\alpha + 2\eta - 2\alpha\eta - 1)) \quad (8.27)$$

Using equation 8.27, we find at the true branching ratio is scaled from  $0.55 \pm 0.03$  to  $0.58 \pm 0.05$ .

## 8.3 $^{15}\text{N}_2$ Titration

Normally  $\text{N}_2$  would not be a good choice, due to the fact that  $\text{N}_2\text{H}^+$  has the same mass as the formyl isomers at  $m/z = 29$ , but we may instead introduce  $^{15}\text{N}_2$  to produce a new peak at  $m/z = 31$ .

### 8.3.1 Estimate Isomerization

To estimate a limit on the isomerization, we consider the above reaction eqs. (8.8) and (8.7), where  $\text{X} = ^{15}\text{N}_2$  in the context that we can only determine the abundance of  $[\text{HCO}]^+$  and  $^{15}\text{N}_2\text{H}^+$ . As a function of pressure, we cannot see reaction 8.8, but if it does contribute, we should see a discrepancy in the total rate constant, which we estimate to be Langevin:  $k_L = 8.0 \times 10^{-10}$ . The functional form is as follows:

$$\eta(t) = C(1 - e^{-k_{8.7}\rho t}) \quad (8.28)$$

Where we define  $\eta(t) \equiv \frac{^{15}\text{N}_2\text{H}^+(t)}{^{15}\text{N}_2\text{H}^+(t) + [\text{HCO}]^+(t)}$

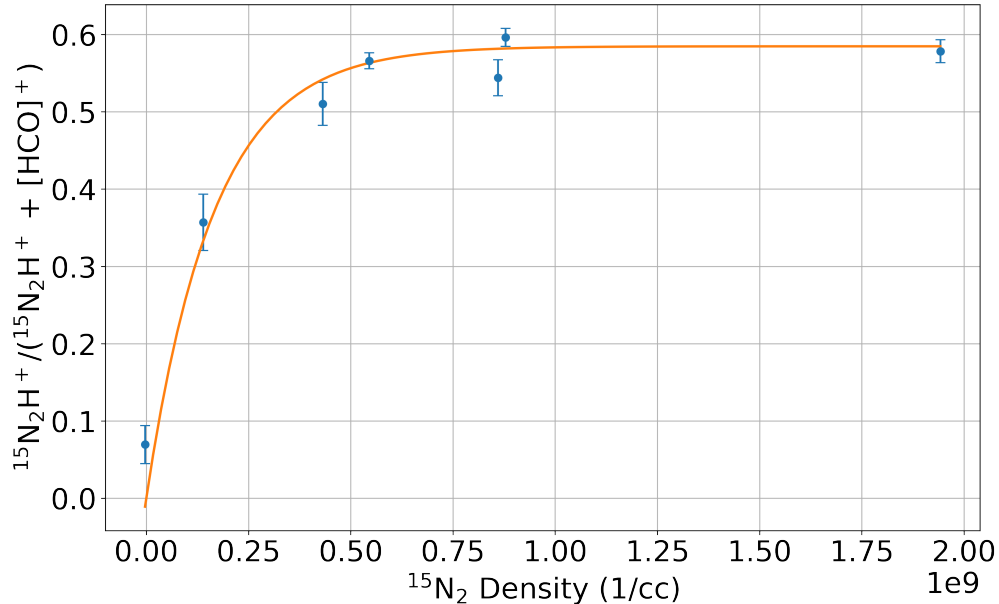


Figure 8.7:  $C = 0.58 \pm 0.02$   $k_{8.7} = ((6.1 \pm 1.5) \times 10^{-10}) \text{ cm}^3/\text{s}$

## CHAPTER 9

### Conclusion and Future Outlook

The experiment has broken new ground in ion-molecule reactions at various reaction temperatures, but there is still much left unexplored. The recent inclusion of two Lioptec dye lasers will allow for more stuff and stuff

## APPENDIX A

### Average Dipole Orientation Theory (ADO)

Adiabatic capture theory is a study of the long range potentials between particles to yield a reaction rate constant. This is easily done for many potentials, such as the ion and induced-dipole interaction (Langevin), but is more difficult when considering potentials with another degree of freedom; in particular, we would like to consider the ion-dipole interaction. Unlike the Langevin interaction, the ion-dipole term has an angular term defined with respect to the inter-molecular axis. A few approximations are taken to give an average dipole orientation theory pioneered and expanded on by Su and Bowers.[47, 48] This can also be extrapolated to include quadrupole interactions.[49]

#### A.0.1 General Treatment of Adiabatic Capture Theory

A general method of calculating the rate constant of two particles with a given potential, finding the collisional cross section, which is then averaged over a velocity distribution to find the rate constant.[59] Starting with the attractive potential, we find that it is a summation of interactions with coefficients  $C_n$  and  $r$  dependence  $n$ .

$$V(r) = \sum_n -\frac{C_n}{r^n} \quad (\text{A.1})$$

In the center of mass frame, we see that

$$V_{eff} = \frac{l^2}{2\mu r^2} - \sum_n \frac{C_n}{r^n} \quad (\text{A.2})$$

if  $n > 2$ , we can derive the capture cross-section and rate constant as follows. First, we

find the position  $r_0$  corresponding to the maximum of the effective potential, which is the maximum of the centrifugal barrier.

$$\frac{\partial V_{eff}(r_0)}{\partial r} = 0$$

$$\therefore r_0 = \left( \frac{n\mu, C_n}{l^2} \right)^{1/n-2}$$

Substituting  $r_0$  back into equation A.2, we find the maximal value of the effective potential:

$$V_{eff}(r_0) = \left( \frac{l^2}{\mu} \right)^{\frac{n}{n-2}} \frac{n-2}{2n} (nC_n)^{-\frac{2}{n-2}} \quad (\text{A.3})$$

This then defines the energy necessary for a collision, for if  $E_{col}$  exceeds  $V_{eff}(r_0)$ , the reactants will be able to surmount the centrifugal barrier and collide. Thus, we may define the maximum value for the angular momentum  $l$  and the impact parameter  $b$ .

$$l_{max} = (\mu n)^{1/2} (C_n)^{1/n} \left( \frac{2E_{col}}{n-2} \right)^{\frac{n-2}{2n}}$$

$$b_{max} = \frac{l_{max}}{\mu v}$$

We can then define a collision cross section dependent on the collision energy:

$$\sigma(E_{col}) = \pi b_{max}^2$$

$$= \frac{\pi}{2} n \left( \frac{2}{n-2} \right)^{\frac{n-2}{2}} \left( \frac{C_n}{E_{col}} \right)^{\frac{2}{n}}$$

Integrating the collision cross section with a Maxwell Boltzmann distribution yields a generalized rate constant as a function of temperature and n.

$$k(T) = \int_0^\infty v f(v) \sigma(v) dv \quad (\text{A.4})$$

$$= \boxed{\sqrt{\frac{2\pi}{\mu}} n \left(\frac{2}{n-2}\right)^{\frac{n-2}{2}} C_n^{2/n} (k_B T)^{\frac{n-4}{2n}} \Gamma\left(2 - \frac{2}{n}\right)} \quad (\text{A.5})$$

### A.0.2 Ion-Dipole Interaction

The Langevin term of the ion and ion-induced dipole interaction is as follows:

$$V_L(r) = -\frac{\alpha q^2}{2r^4} \quad (\text{A.6})$$

In the case of the ion-dipole interaction:

$$V_D(r, \theta) = -\frac{q\mu_D}{r^2} \cos(\theta) \quad (\text{A.7})$$

The method outlined in section A.0.1 finds the rate constant by dealing with a two body problem only needing to consider the  $r$  degree of freedom. The inclusion of the  $\theta$  term complicates this, but to first order, we can parameterize it as a function of  $r$ . What we want to achieve is to write down the potential as such:

$$\begin{aligned} V(r) &= -\frac{\alpha q^2}{2r^4} - \frac{q\mu_D}{r^2} \cos(\bar{\theta}(r)) \\ \bar{\theta} &= \frac{\int \theta P(\theta) d\theta}{\int P(\theta) d\theta} \end{aligned} \quad (\text{A.8})$$

Where  $P(\theta)$  is the probability of finding the dipole at  $\theta$ . To determine the average orientation of the dipole, we consider the following cases:

1.  $P(\theta)$  is inversely proportional to the angular velocity:

$$P(\theta) \propto 1/\dot{\theta}$$

2. An orientation has a probability weighted by the circumference of an angle:

$$C = 2\pi l \sin(\theta)$$

$$P(\theta) \propto \sin(\theta)$$

The angular probability is proportional to both effects:

$$P(\theta) \propto \frac{\sin(\theta)}{\dot{\theta}} \quad (\text{A.9})$$

We can relate the angular velocity to the angular kinetic energy and the total energy in the system:

$$\begin{aligned} KE_{rot} &= \frac{1}{2} I \dot{\theta}^2 \\ E_{tot} &= KE_{rot} + V_D \end{aligned} \quad (\text{A.10})$$

Redefining equation A.9 with equation A.10, we find:

$$P(\theta) \propto \frac{\sin(\theta)}{\sqrt{E_{rot} - V_D}} \quad (\text{A.11})$$

Combining equations eqs. (A.11) and (A.8) yields a total averaged dipole orientation.

$$\bar{\theta} = \frac{\int \frac{\theta \sin(\theta) d\theta}{\sqrt{E_{rot} + q\mu_D/r^2 \cos(\theta)}}}{\int \frac{\sin(\theta) d\theta}{\sqrt{E_{rot} + q\mu_D/r^2 \cos(\theta)}}} \quad (\text{A.12})$$

From here, two situations arise:

1.  $E_{rot} = E_1 < \frac{q\mu_D}{r^2}$ : There is not enough rotational energy to overcome the dipole locking. The solution is oscillatory, but  $\theta$  has an  $r$  dependent bound. We let the maximal capture angle be defined as  $K$ .

$$E_1 = -\frac{q\mu_D}{r^2} \cos(K)$$

When substituted into equation A.12, we find:

$$\bar{\theta}_1 = \frac{\int_0^K \frac{\theta \sin(\theta) d\theta}{\sqrt{\cos(\theta) - \cos(K)}}}{\int_0^K \frac{\sin(\theta) d\theta}{\sqrt{\cos(\theta) - \cos(K)}}}$$

After some math (something something integration by infinite series) and get a result of:

$$\bar{\theta}_1 = \frac{2\sqrt{2}A}{\sqrt{1 - \cos(K)}}$$

where  $A \equiv \int_0^{\pi/2} \frac{a^2 \cos(\phi)^2 d\phi}{\sqrt{q - a^2 \sin(\phi)^2}}$

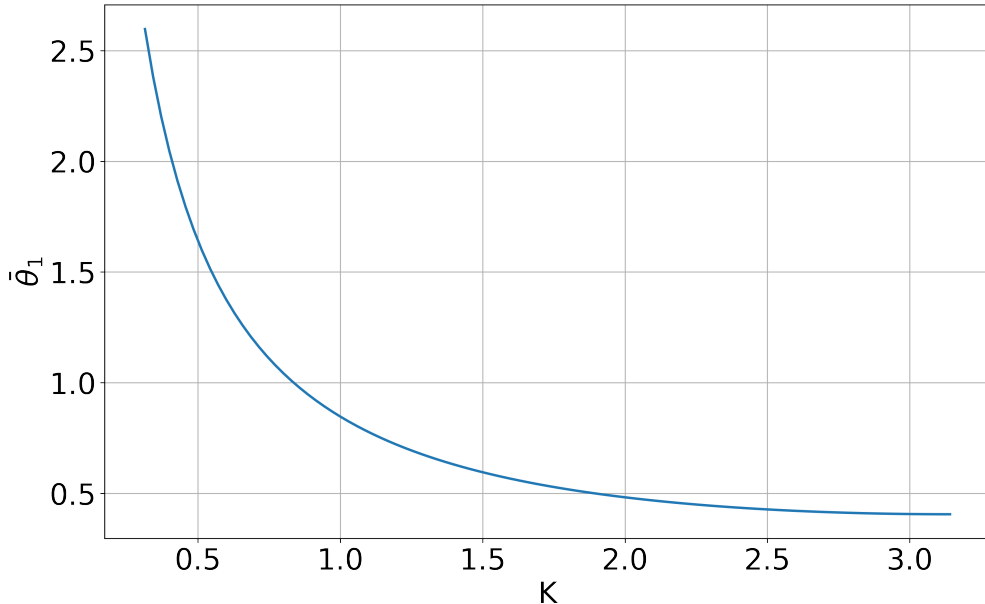


Figure A.1: Rough plotting of  $\theta_1$  as a function of maximum angle  $K$ . The behaviour is as expected, the greater the maximal capture angle, the more  $\theta_1$  tends towards 0.

2.  $E_{rot} = E_1 > \frac{q\mu_D}{r^2}$ : The rotational energy is enough to overcome the dipole locking and

$\theta$  can swing around in a complete circle

$$\bar{\theta}_2 = \frac{\int_0^\pi \frac{\theta \sin(\theta) d\theta}{\sqrt{E_2 + q\mu_D/r^2 \cos(\theta)}}}{\int_0^\pi \frac{\sin(\theta) d\theta}{\sqrt{E_2 + q\mu_D/r^2 \cos(\theta)}}} \quad (\text{A.13})$$

We no longer have bounds on the angles the dipole is allowed over, but the behavior is still dependent on the strength of the internal energy and dipole force.

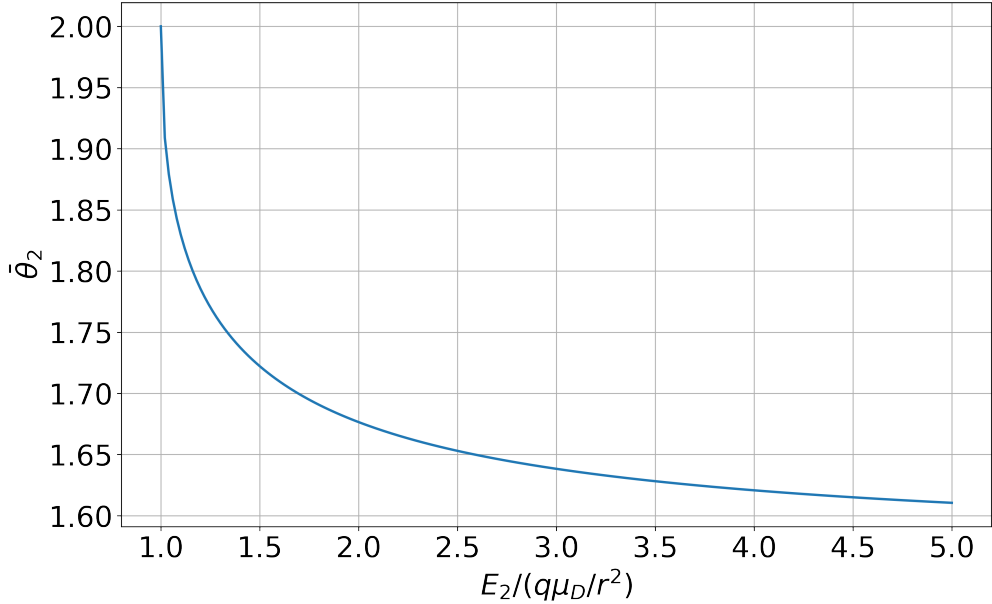


Figure A.2:  $\theta_2$  as a function of the ratio of rotational energy and the monopole-dipole term. The low ratio behavior is not immediately obvious, but the greater the ratio between the rotational energy and monopole-dipole term, the more  $\theta_2$  tends towards  $\pi/2$ .

Let's say we have the forms for  $\bar{\theta}_1$  and  $\bar{\theta}_2$ , we want to write down the full form of  $\theta$ . We can combine the two weighted by the probability of each as a function of internal energy.

$$\bar{\theta}(r) = \bar{\theta}_1(r)F_1 + \bar{\theta}_2(r)F_2$$

Where these weightings are found via:

$$P(\epsilon)d\epsilon = \frac{1}{k_B T} e^{-\frac{\epsilon}{k_B T}} d\epsilon$$

For diatomics, we can use:

$$\epsilon = \frac{J(J+1)\hbar^2}{2I}$$

We can then use equation A.4 and get a cross section and rate constant. The form is similar to that of just a Langevin term, but now with a dipole interaction term added onto it. All of the terms aside from  $C$  come from the integration over a Boltzmann distribution, where then averaging over the angles is wrapped up into the  $C$  term.

$$k_{ADO} = \frac{2\pi e}{\sqrt{\mu}} \left( \sqrt{\alpha} + C\mu_D \sqrt{\frac{2}{\pi k_B T}} \right) \quad (\text{A.14})$$

The dipole locking constant ( $C$ ) can be numerically solved by iteratively integrating over combinations of  $\mu_D$  and  $\alpha$ .[47][51]

## APPENDIX B

### Statistical State Counting

$$E_{int} = \omega_e \left( v + \frac{1}{2} \right) - \omega_e x_e \left( v + \frac{1}{2} \right)^2 + B_e j(j+1) \quad (\text{B.1})$$

Where  $\omega_e$  is the vibrational constant,  $\omega_e x_e$  is the anharmonic vibrational constant,  $B_e$  is the rotational constant, and  $v, j$  are vibrational and rotational quantum numbers respectively. You can count how many states there are up to a maximum energy input and compare states to see which product channel is preferred statistically.

To get a more accurate counting, we should be comparing the integrated states including the energy taken away by the other reactant.

$$\int_0^{p_{max}} 4\pi p^2 n(p) dp \quad (\text{B.2})$$

where  $n(p)$  is the number of internal states allowed with momentum  $p$

## REFERENCES

- [1] N. G. Adams and D. Smith. The selected ion flow tube (SIFT); A technique for studying ion-neutral reactions. *International Journal of Mass Spectrometry and Ion Physics*, 21(3-4):349–359, 1976.
- [2] Marcelino Agúndez and Valentine Wakelam. Chemistry of Dark Clouds: Databases, Networks, and Models. *Chemical Reviews*, 113(12):8710–8737, 2013.
- [3] PB Armentrout. Reactions and Thermochemistry of Small Transition Metal Cluster Ions. *Annual Review of Physical Chemistry*, 52(1):423–461, 2002.
- [4] J J Bollinger, J S Wells, D J Wineland, and Wayne M Itano. Hyperfine structure of the  $2p^2P_{1/2}$  state in  ${}^9\text{Be}^+$ . *Physical Review A*, 31(4):2711–2714, 1985.
- [5] Michael J. Bronikowski, William R. Simpson, Bertrand Girard, and Richard N. Zare. Bond-specific chemistry: OD:OH product ratios for the reactions H+HOD(100) and H+HOD(001). *Journal of Chemical Physics*, 95(11):8647–8648, 1991.
- [6] Eduardo Carrascosa, Jennifer Meyer, and Roland Wester. Imaging the dynamics of ion-molecule reactions. *Chemical Society Reviews*, 46(24):7498–7516, 2017.
- [7] Kuang Chen, Scott T. Sullivan, and Eric R. Hudson. Neutral gas sympathetic cooling of an ion in a Paul trap. *Physical Review Letters*, 112(14):1–5, 2014.
- [8] Kuang Chen, Scott T. Sullivan, Wade G. Rellergert, and Eric R. Hudson. Measurement of the coulomb logarithm in a radio-frequency Paul trap. *Physical Review Letters*, 110(17):1–5, 2013.
- [9] D. C Clary. Fast Chemical Reactions: Theory Challenges Experiment. *Annual Review of Physical Chemistry*, 41(1):61–90, 1990.
- [10] F. Fleming Crim. Bond-selected chemistry: Vibrational state control of photodissociation and bimolecular reaction. *Journal of Physical Chemistry*, 100(31):12725–12734, 1996.
- [11] N. F. Dalleska, Kevin C. Crellin, and P. B. Armentrout. Reactions of alkaline earth ions with hydrogen, deuterium, and hydrogen deuteride. *The Journal of Physical Chemistry*, 97(13):3123–3128, 2005.
- [12] C. E. Dateo and D. C. Clary. Rate constant calculations on the  $\text{C}^+ + \text{HCl}$  reaction. *The Journal of Chemical Physics*, 1989.
- [13] Colin G. Freeman, John S. Knight, Jonathan G. Love, and Murray J. McEwan. The reactivity of  $\text{HOC}^+$  and the proton affinity of CO at O. *International Journal of Mass Spectrometry and Ion Processes*, 80(C):255–271, 1987.

- [14] Colin G. Freeman and Murray J. McEwan. A selected-ion flow tube study of the  $\text{C}^+ + \text{H}_2\text{O}$  reaction. *International Journal of Mass Spectrometry and Ion Processes*, 75(1):127–131, 1987.
- [15] Bina Fu and Dong H. Zhang. A full-dimensional quantum dynamics study of the mode specificity in the  $\text{H} + \text{HOD}$  abstraction reaction. *Journal of Chemical Physics*, 142(6), 2015.
- [16] George Gioumousis and D. P. Stevenson. Reactions of gaseous molecule ions with gaseous molecules. V. theory. *The Journal of Chemical Physics*, 29(2):294–299, 1958.
- [17] Anders K. Hansen, Magnus A. Sørensen, Peter F. Staanum, and Michael Drewsen. Single-ion recycling reactions. *Angewandte Chemie - International Edition*, 51(32):7960–7962, 2012.
- [18] William L. Hase, Jochen Mikosch, Roland Wester, Jiaxu Zhang, Rico Otto, and Jing Xie. Identification of Atomic-Level Mechanisms for Gas-Phase  $\text{X}^- + \text{CH}_3 \rightarrow \text{S}_{\text{N}}2$  Reactions by Combined Experiments and Simulations. *Accounts of Chemical Research*, 47(10):2960–2969, 2014.
- [19] J L Highberger, C Savage, J H Bieging, and L M Ziurys. HEAVY-METAL CHEMISTRY IN PROTO-PLANETARY NEBULAE: DETECTION OF MgNC, NaCN, AND AlF TOWARD CRL 2688. *the Astrophysical Journal*, 562:790–798, 2001.
- [20] Eric R. Hudson. Sympathetic cooling of molecular ions with ultracold atoms. *EPJ Techniques and Instrumentation*, 3(1):8, 2016.
- [21] W. T. Huntress and R. F. Pinizzotto. Product distributions and rate constants for ion-molecule reactions in water, hydrogen sulfide, ammonia, and methane. *The Journal of Chemical Physics*, 59(9):4742–4756, 2004.
- [22] Nicholas R Hutzler, Hsin-I Lu, and John M Doyle. The buffer gas beam: an intense, cold, and slow source for atoms and molecules. *Chemical reviews*, 112(9):4803–27, sep 2012.
- [23] NR Nicholas R Hutzler, MF Maxwell F Parsons, Yulia V Gurevich, Paul W Hess, Elizabeth Petrik, Ben Spaun, Amar C Vutha, David Demille, Gerald Gabrielse, and John M Doyle. A cryogenic beam of refractory, chemically reactive molecules with expansion cooling. . . . *Chemistry Chemical . . . ,* 13(42):1–16, 2011.
- [24] Vladimir A Krasnopolsky. Chemical composition of Titan’s atmosphere and ionosphere: Observations and the photochemical model. *Icarus*, 236:83–91, 2014.
- [25] D. J. Larson, J. C. Bergquist, J. J. Bollinger, Wayne M. Itano, and D. J. Wineland. Sympathetic cooling of trapped ions: A laser-cooled two-species nonneutral ion plasma. *Physical Review Letters*, 57(1):70–73, 1986.

- [26] Adan Li, Jianzheng Song, Yang Sun, and Tifeng Jiao. The application of resonance-enhanced multiphoton ionization technique in gas chromatography mass spectrometry. *Journal of Spectroscopy*, 2014, 2014.
- [27] Jun Li, Bin Jiang, and Hua Guo. Spin-orbit corrected full-dimensional potential energy surfaces for the two lowest-lying electronic states of  $\text{FH}_2\text{O}$  and dynamics for the  $\text{F} + \text{H}_2\text{O} \rightarrow \text{HF} + \text{OH}$  reaction. *Journal of Chemical Physics*, 138(7), 2013.
- [28] Jun Li, Bin Jiang, Hongwei Song, Jianyi Ma, Bin Zhao, Richard Dawes, and Hua Guo. From ab initio potential energy surfaces to state-resolved reactivities:  $\text{X} + \text{H}_2\text{O} \leftrightarrow \text{HX} + \text{OH}$  [ $\text{X} = \text{F}, \text{Cl}$ , and  $\text{O}({}^3\text{P})$ ] reactions. *Journal of Physical Chemistry A*, 119(20):4667–4687, 2015.
- [29] U. Lourderaj, M. Weidemuller, W. L. Hase, J. Mikosch, R. Otto, R. Wester, C. Eichhorn, J. X. Zhang, and S. Trippel. Imaging Nucleophilic Substitution Dynamics. *Science*, 319(5860):183–186, 2008.
- [30] Ricardo B. Metz, John D. Thoemke, Joann M. Pfeiffer, and F. Fleming Crim. Selectively breaking either bond in the bimolecular reaction of  $\text{HOD}$  with hydrogen atoms. *Journal of Chemical Physics*, 99(3):1744–1751, 1993.
- [31] Edvardas Narevicius, Adam Libson, Christian G. Parthey, Isaac Chavez, Julia Narevicius, Uzi Even, and Mark G. Raizen. Stopping supersonic oxygen with a series of pulsed electromagnetic coils: A molecular coilgun. *Physical Review A - Atomic, Molecular, and Optical Physics*, 77(5):1–4, 2008.
- [32] M. Oppenheimer and A. Dalgarno. The Fractional Ionization in Dense Interstellar Clouds. *The Astrophysical Journal*, 192(12):29, 2002.
- [33] Hans Pauly. *Atom, Molecule, and Cluster Beams I: Basic Theory, Production and Detection of Thermal Energy Beams*, volume 28. Springer, 2000.
- [34] Prateek Puri, Michael Mills, Christian Schneider, Ionel Simbotin, John A. Montgomery, Robin Côté, Arthur G. Suits, and Eric R. Hudson. Synthesis of mixed hypermetallic oxide  $\text{BaO}\text{Ca}^+$  from laser-cooled reagents in an atom-ion hybrid trap. *Science*, 357(6358):1370–1375, 2017.
- [35] Amelia W. Ray, Jianyi Ma, Rico Otto, Jun Li, Hua Guo, and Robert E. Continetti. Effects of vibrational excitation on the  $\text{F} + \text{H}_2\text{O} \rightarrow \text{HF} + \text{OH}$  reaction: Dissociative photodetachment of overtone-excited  $[\text{F}-\text{H}-\text{OH}]^-$ . *Chemical Science*, 8(11):7821–7833, 2017.
- [36] B. Roth, P. Blythe, H. Wenz, H. Daerr, and S. Schiller. Ion-neutral chemical reactions between ultracold localized ions and neutral molecules with single-particle resolution. *Physical Review A - Atomic, Molecular, and Optical Physics*, 73(4):1–9, 2006.

- [37] Christian Schneider, Steven J. Schowalter, Kuang Chen, Scott T. Sullivan, and Eric R. Hudson. Laser-Cooling-Assisted Mass Spectrometry. *Physical Review Applied*, 2(3):1–7, 2014.
- [38] Steven J. Schowalter, Kuang Chen, Wade G. Rellergert, Scott T. Sullivan, and Eric R. Hudson. An integrated ion trap and time-of-flight mass spectrometer for chemical and photo- reaction dynamics studies. *Review of Scientific Instruments*, 83(4), 2012.
- [39] Steven J. Schowalter, Alexander J. Dunning, Kuang Chen, Prateek Puri, Christian Schneider, and Eric R. Hudson. Blue-sky bifurcation of ion energies and the limits of neutral-gas sympathetic cooling of trapped ions. *Nature Communications*, 7:1–8, 2016.
- [40] Ian R Sims. Gas-Phase Reactions and Energy Transfer at Very Low Temperatures. *Annual Review of Physical Chemistry*, 46(1):109–137, 2002.
- [41] Amitabha Sinha, Mark C. Hsiao, and F. Fleming Crim. Bond-selected bimolecular chemistry:  $\text{H} + \text{HOD}(4\nu_{OH}) \rightarrow \text{OD} + \text{H}_2$ . *The Journal of Chemical Physics*, 92(10):6333–6335, 1990.
- [42] Dimitris Skouteris, David E. Manolopoulos, Wensheng Bian, Hans Joachim Werner, Lih Huey Lai, and Kopin Liu. Van der Waals interactions in the Cl + HD reaction. *Science*, 286(5445):1713–1716, 1999.
- [43] I. W M Smith and Bertrand R. Rowe. Reaction kinetics at very low temperatures: Laboratory studies and interstellar chemistry. *Accounts of Chemical Research*, 33(5):261–268, 2000.
- [44] Theodore P. Snow and Veronica M. Bierbaum. Ion Chemistry in the Interstellar Medium. *Annual Review of Analytical Chemistry*, 1(1):229–259, 2008.
- [45] Hongwei Song and Hua Guo. Vibrational and Rotational Mode Specificity in the Cl + H<sub>2</sub>O → HCl + OH Reaction: A Quantum Dynamical Study. *Journal of Physical Chemistry A*, 119(24):6188–6194, 2015.
- [46] Hongwei Song, Soo Ying Lee, Yunpeng Lu, and Hua Guo. Full-Dimensional Quantum Dynamical Studies of the Cl + HOD → HCl/DCl + OD/OH Reaction: Bond Selectivity and Isotopic Branching Ratio. *Journal of Physical Chemistry A*, 119(50):12224–12230, 2015.
- [47] Timothy Su and Michael T. Bowers. Ion-polar molecule collisions: the effect of ion size on ion-polar molecule rate constants; the parameterization of the average-dipole-orientation theory. *International Journal of Mass Spectrometry and Ion Physics*, 12(4):347–356, 1973.
- [48] Timothy Su and Michael T. Bowers. Theory of ion-polar molecule collisions. Comparison with experimental charge transfer reactions of rare gas ions to geometric isomers of difluorobenzene and dichloroethylene. *The Journal of Chemical Physics*, 58(7):3027–3037, 1973.

- [49] Timothy Su and Michael T. Bowers. Ion-polar molecular collisions: the average quadrupole orientation theory. *International Journal of Mass Spectrometry and Ion Physics*, 17(3):309–319, 1975.
- [50] Michał Tomza, Krzysztof Jachymski, Rene Gerritsma, Antonio Negretti, Tommaso Calarco, Zbigniew Idziaszek, and Paul S. Julienne. Cold hybrid ion-atom systems. pages 1–61, 2017.
- [51] J. Troe. Statistical adiabatic channel model of ion-neutral dipole capture rate constants. *Chemical Physics Letters*, 122(5):425–430, 1985.
- [52] Ewine F. van Dishoeck, Eric Herbst, and David A. Neufeld. Interstellar Water Chemistry: From Laboratory to Observations. *Chemical Reviews*, 113(12):9043–9085, 2013.
- [53] Stefan Willitsch. Coulomb-crystallised molecular ions in traps: Methods, applications, prospects. *International Reviews in Physical Chemistry*, 31(2):175–199, 2012.
- [54] D. J. Wineland and Wayne M. Itano. Laser cooling of atoms. *Physical Review A*, 20(4):1521–1540, 1979.
- [55] Paul Wolfgang. Electromagnetic Traps For charged And Neutral Particles, 1990.
- [56] Chunlei Xiao, Xin Xu, Shu Liu, Tao Wang, Wenrui Dong, Tiangang Yang, Zhigang Sun, Dongxu Dai, Xin Xu, Dong H Zhang, and Xueming Yang. Experimental and theoretical differential cross sections for a four-atom reaction:  $\text{HD} + \text{OH} \rightarrow \text{H}_2\text{O} + \text{D}$ . *Science*, 333(6041):440–442, 2011.
- [57] Richard N. Zare. Laser Control of Chemical Reactions. *Science*, 279(5358):1875–1879, 1998.
- [58] Dong H Zhang and John C Light. Full-dimensional quantum study. 93(5):691–697, 1997.
- [59] Dongdong Zhang and Stefan Willitsch. Cold ion chemistry. 2017.
- [60] Rui Zheng, Yongfa Zhu, and Hongwei Song. Mode specific dynamics in bond selective reaction  $\text{O}'(^3\text{P}) + \text{HOD} \rightarrow \text{O}'\text{H} + \text{OD}/\text{O}'\text{D} + \text{OH}$ . *Journal of Chemical Physics*, 149(5), 2018.